

International Journal of Modern Physics D
 © World Scientific Publishing Company

Understanding the Very High-Energy Emission from Microquasars

Valentí Bosch-Ramon

Dmitry Khangulyan

*Max Planck Institut für Kernphysik, postfach 10 39 80 69029 Heidelberg, Germany
 Valenti.Bosch-Ramon@mpi-hd.mpg.de/Dmitry.Khangulyan@mpi-hd.mpg.de*

Received Day Month Year

Revised Day Month Year

Communicated by Managing Editor

Microquasars are X-ray binaries with relativistic jets. These jets are powerful energy carriers, thought to be fed by accretion, which produce non-thermal emission at different energy bands. The processes behind the bulk of the non-thermal emission in microquasars may be of leptonic (synchrotron and inverse Compton) and hadronic (proton-proton interactions, photo-meson production, and photo-disintegration) nature. When leptonic, the fast particle cooling would allow the obtention of relevant information about the properties close to the accelerator, like the radiation and the magnetic field energy densities, and the acceleration efficiency. When hadronic, the extreme conditions required in the emitter would have strong implications on the physics of jets and their surroundings. The very high-energy part of the spectrum, i.e. > 100 GeV, is a good energy range to explore the physics behind the non-thermal radiation in these compact variable sources. In addition, this energy range, when taken altogether with lower energy bands, is a key piece to construct a comprehensive picture of the processes occurring in the emitter. Until recently, the very high-energy range was hard to probe due to the lack of sensitivity and spatial and spectral resolution of previous instrumentation. Nowadays, however, powerful gamma-ray instruments are operating and the quality of their observations is allowing, for the first time, to start to understand the production of high-energy emission in microquasars.

To date, several Galactic sources showing extended radio emission, among them at least one confirmed microquasar, Cygnus X-1, have shown a TeV signal. All of them show complex patterns of spectral and temporal behavior. In this work, we discuss the physics behind the very high-energy emission in the microquasar Cygnus X-1, and also in the other two TeV binaries with detected extended outflows, LS 5039 and LS I +61 303, pointing out relevant aspects of the complex phenomena occurring in them. We conclude that the TeV emission is likely of leptonic origin, although hadrons cannot be discarded. In addition, efficient electromagnetic cascades can hardly develop since even relatively low magnetic fields suppress them. Also, the modeling of the radiation from some of the detected sources points to them as either extremely efficient accelerators, and/or having the TeV emitter at a distance from the compact object of about $\sim 10^{12}$ cm. Finally, we point out that the role of a massive and hot stellar companion, due to its strong photon field and wind, cannot be neglected when trying to understand the behavior of microquasars at high and very high energies. The complexity of microquasars precludes straightforward generalizations to a whole population, and are better studied presently in a source by source base. The new and future gamma-ray instrumentation will imply a big step further in our understanding of the processes in microquasars and gamma-ray

2 *V. Bosch-Ramon & D. Khangulyan*

emitting binaries.

Keywords: Microquasars; radiative processes; outflows; gamma-ray emission

1. Introduction

Microquasars are an X-ray binary (XRB) subclass formed by those sources that present extended radio jets (e.g. Mirabel & Rodríguez ¹). These systems are formed by a non-degenerated star, which can be in different stages of its evolution, and a compact object, which can be a black-hole or a neutron star. Depending on the mass of the non-degenerated stellar companion, the system is considered a low or a high-mass microquasar. Typically, systems harboring an OB star are considered high-mass XRBs (HMXB), and XRBs with later type stellar companions are classified as intermediate or low-mass XRBs. It is thought that the compact object powers the relativistic jets via accretion of matter expelled from the companion. This material, when reaching the surroundings of the compact object, forms an accretion disk that is usually detected in the X-rays. Simplifying very much the case, depending on the accretion state, the X-ray spectrum varies strongly, from a multi-color black body peaking around 1 keV plus a minor soft power-law spectrum at higher energies, for high accretion rates (high-soft state), to one dominated by a hard power-law spectrum plus an exponential cutoff around 100 keV, for low accretion rates (low-hard state; for an extensive description of the X-ray phenomenology, see McClintock & Remillard ²). It is expected that a persistent jet will be present during the low-hard state, and a transient ejection will form when switching from the low-hard to the high-soft state (Fender et al. ³). Correlations between the radio and the X-ray luminosity, and the accretion/ejection activity, have been proposed (e.g. Gallo et al. ⁴, Corbel et al. ⁵, Fender et al. ⁶).

The jet formation and the production of non-thermal radiation in the jet are major ingredients that distinguish a microquasar among other types of XRBs. The non-thermal radiation produced in microquasar jets has been resolved in radio at very different spatial scales (e.g. Ribó ⁷) and also in X-rays at large scales (e.g. Corbel et al. ⁸). This emission is a clear evidence that particle acceleration takes place in different locations of microquasar jets under very different conditions (for a discussion on this, see, e.g., Bosch-Ramon ⁹). There are also radio emitting XRBs in which extended emission has not been detected. It has been proposed that these sources could be microquasars as well (e.g. Fender ¹⁰), like the low-mass system XTE J1118+480 (e.g., Chaty et al. ¹¹), the jet of which has not been resolved yet.

Microquasars show up themselves as compact and rapidly variable sources from radio to very high energies. In such a type of emitters, when radiating particles are leptons, the highest energy part of the spectrum is a good range to explore non-thermal processes. It is due to the short timescales associated to the particles that produce the emission, which implies that the accelerator and the emitter are likely the same or similar regions. In case of hadrons, it is possible to derive important information concerning the jet hadronic content, at least of its relativistic part,

whereas at the same time it is giving information of the conditions of the emitter, like very dense matter and/or target photon fields. Moreover, photons generated by very high-energy (VHE) electrons and/or protons give a better insight on the mechanism of acceleration and the conditions under which it takes place, helping to understand better the processes that accelerate particles up to such high energies. Finally, the presence of a hot and massive star renders a scenario in which photon-photon absorption, and the occurrence of electromagnetic cascades, can be studied. This can give important information on the conditions of the massive star surroundings.

Historically, the poor spatial resolution and sensitivity of the available instruments working at gamma-ray energies were not enough for accurate theoretical modeling, although these sources were proposed to be gamma-ray emitters more than a decade ago (e.g. Levinson & Blandford ¹²; Levinson & Mattox ¹³; Paredes et al. ¹⁴). Nowadays, however, powerful gamma-ray instruments are operating or will start soon, and the quality of their observations is allowing us, for the first time, to probe the physical processes that take place in microquasars and their jets. These observations at very high energies give the necessary input to constrain the theoretical models that lacked in the past.

The recent evidence of detection of a transient event, at the (post-trial) significance level of 4.1σ , from Cygnus X-1 (Albert et al. ¹⁵) have shown that microquasars can indeed produce VHE emission, and VHE observations can bring to us important information on these sources. Another two interesting cases are LS 5039 and LS I +61 303. The former has been detected in the TeV range by the Cherenkov telescope HESS (Aharonian et al. ¹⁶), showing a periodic behavior in the VHE radiation (Aharonian et al. ¹⁷) with the same period as the orbit (Casares et al. ¹⁸). LS I +61 303 has been also detected at TeV energies by the Cherenkov telescope MAGIC, being its emission variable (Albert et al. ¹⁹). Unlike Cygnus X-1, which is a firmly established microquasar, LS 5039 and LS I +61 303 are no considered at present microquasars due to some peculiarities in their X-ray and radio characteristics. Nevertheless, both sources present, like Cygnus X-1, extended radio emission, and harbor OB stars.

In this review, we want to take profit of the new microquasar phenomenology at very high energies, to draw a theoretical picture of the non-thermal processes that could take place in these sources. This is to be put in the context of the historical evolution of the field, which will be summarized. To explore which are the relevant processes in the microquasar scenario, we will carry out a detailed review of different mechanisms: particle transport, radiation and photon-photon absorption, in the context of microquasars. Using this sound and basic theoretical background, plus the observational knowledge at very high energies from the sources presented above, the microquasar Cygnus X-1, and also the TeV binaries LS 5039 and LS I +61 303, constraints on their physical conditions will be inferred. We note that the type of approach applied to these sources is applicable to large extent to any close binary system emitting in the TeV regime. It is worth mentioning here a recent review

4 *V. Bosch-Ramon & D. Khangulyan*

of a broader topic by Levinson⁽²⁸⁾ on VHE radiation from jets including active galactic nuclei, gamma-ray bursts, and microquasars. It is also interesting to note that massive young stellar objects, also presenting jets, have been proposed to be gamma-ray emitters by Araudo et al.⁽²⁹⁾.

This work is organized in the following manner. In Sections 2 and 3, we try to look comprehensively at the microquasar phenomenological picture, setting up a general scenario for these sources. In addition, there we summarize in a non-exhaustive way previous studies of different topics related to microquasars at high energies. In Sect. 4, a short review on different particle transport, acceleration and radiation mechanisms is done, treating also briefly the issue of gamma-ray absorption and electromagnetic cascading in microquasars. All this can help to understand how the new VHE data fits in previous ideas and frameworks. Also, we put forward a plain but physically sound leptonic model to explore the processes that are involved in the generation and absorption of VHE emission in jet galactic sources, trying to understand which kind of physics is relevant there. For this, the recent observational findings at very high energies concerning microquasars are used. In Sect. 5, some hot topics of the field are discussed with some extension. Finally, in Sect. 6, the main ideas of this work are summarized.

2. The study of microquasars

At the discovery of microquasars, their physics was object of speculation due to the morphological similarities of these sources with their larger scale analogs, the quasars (Mirabel et al.²⁰). The question was to find out to which extent the processes taking place in extragalactic jet sources could be extended to galactic ones. In addition to morphology, kinematical similarities became apparent when superluminal moving ejecta were found at radio wavelengths in GRS 1915+150 (Mirabel et al.²¹). Nowadays it is widely spread the opinion that galactic and extragalactic relativistic jet sources share much more than just morphological and kinematical resemblance. In fact, since both types of source harbor a compact object surrounded by an accretion disk and a relativistic outflow that is an efficient non-thermal emitter, the original analogy argument has been extended not only to the mechanisms that are producing such non-thermal radiation but even beyond. The aim would be to embrace also the physical link between the relativistic particle generation, the accretion phenomena, the jet formation and to some extent the interaction between the jet and its environment. A well known example would be the phenomenological scaling laws relating the physics of the radio and the X-ray emission in microquasars with the accretion rate (e.g. Corbel et al.⁵; Gallo et al.⁴), and its more general version that includes the mass of the black-hole, being extended to extragalactic objects (e.g. Merloni et al.²²; Falcke et al.²³; Körding et al.²⁴). As already mentioned, these empirical scaling laws include the accretion rate and the central object mass as the key parameters to account for (at some stage Doppler boosting is to be added), as well as phenomenological links, sometimes accretion and

jet formation theory motivated, between the radio, the X-ray, and the jet kinetic luminosities and the accretion rate itself.

It is usual and seems natural to associate the properties of the accretion disk, the jet and the compact object mass. The latter will influence strongly the properties of the infalling matter, like the accretion rate, the accreted matter temperature, the magnetic field strength or the accretion disk radiative output. In many XRBs, standard accretion theory can explain the X-ray spectrum quite accurately via thermal emission from the inner parts of the accretion disk plus a corona-like emitter^a, although there is an on-going debate concerning the origin of the hard X-rays, whether they come from the jet base, or from a corona-like region close to the compact object, both of similar properties (e.g. Markoff et al. ²⁵; Maccarone ²⁶). In any case, some sources do not fit in any of these schemas, since their X-ray radiation does not seem to come from the regions close to the compact object but further out, like the case of SS 433 and, perhaps as well, LS 5039 and LS I +61 303. This could be explained by recent theoretical studies that show that the role of the magnetic field can be more crucial than the compact object mass itself and can lead to radiatively inefficient accretion (Bogovalov & Kelner ²⁷), in which case the jet could dominate in the X-ray band (see also Fender et al. ⁶).

Theoretically, the relationship between the compact object mass and the jet physics (e.g. ejected mass rate, matter content, internal energy, carried magnetic energy, bulk speed) is unclear since the accretion/ejection physics is not well known. Furthermore, the link between the main jet properties and the production of non-thermal particles and their radiation cannot be based on first principles, since it relies on the particular conditions of the jet plasma (sound speed, diffusion coefficients, local magnetic field, degree of turbulence, presence of shocks and their velocity, radiation field, plasma density and temperature, etc.), which are not properly constrained. Actually, the situation is even more complicated due to the influence on the jet processes and the non-thermal radiation itself of external factors like, for instance, an external radiation field, the wind produced by the star, the properties of the interstellar medium (ISM), etc. Therefore, although empirical laws can help to classify objects via significant features of their emission and be powerful heuristic tools, it is sometimes difficult to motivate them from first principles, and fundamental approaches become necessary. Such fundamental approaches have to be applied source by source and grounded on detailed observational data. It requires keeping a comprehensive approach to study the source (i.e. phenomenological studies), but developing more fundamental theoretical models.

3. High energy processes in microquasars: a historical perspective

In this section, a schematic and descriptive picture for the relevant processes taking place in microquasars, like particle acceleration, and generation and absorption of

^aA region surrounding the compact object that would be filled with a hot population of electrons and ions.

VHE radiation, is presented together with a historical perspective of the field. This will set up the context within which a more detailed physical treatment will be carried out in Sect. 4.

3.1. A descriptive picture

For illustrative purposes, we show in Figure 1 a very schematic picture of a micro-quasar together with its main elements, and some of the processes taking place in these objects. Some regions of the jet are labeled depending on the main radiative products. This simplified picture would consist on several important elements: the companion star, the stellar radiation field, the stellar wind, the compact object, the accretion disk, and the jet itself. The relativistic particles inside the jet will interact with the stellar radiation field as well as the jet magnetic field producing inverse Compton (IC) and synchrotron radiation, respectively. Under the strong stellar radiation field, the creation of pairs will be unavoidable if VHE gamma-rays are produced. Finally, the stellar wind may have a significant impact on the jet. All this, plus some additional physical processes (not included in Fig. 1 for clarity), like hadronic emission, will be discussed in more detail in Sect. 4.

3.2. Jet formation, evolution and termination

We present here a brief description of a plausible picture for the jet development, from the launching to the termination point.

Although a complete theory for jet generation is still lacking, many studies on jet powering, acceleration and collimation have been carried out during the last

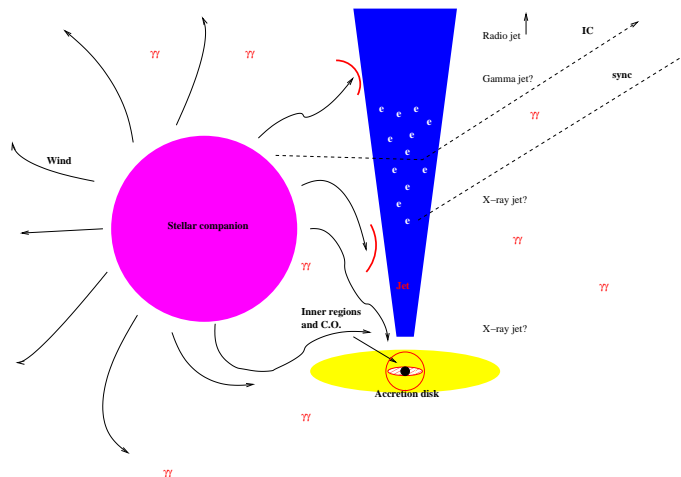


Fig. 1. A sketch of a microquasar. We explicitly show the star, the stellar wind, the accretion disk, the jet, the jet relativistic electrons, some leptonic radiation processes, and pair creation under the stellar photon field.

decades (e.g. Blandford ³⁰; Blandford & Znajek ³¹; Blandford & Payne ³²; Meier ³³; Koide et al. ³⁴; Chattopadhyay & Chakrabarti ³⁵; Meier ³⁶; Hujeirat ³⁷; Meier ³⁸; Bogovalov & Kelner ²⁷; De Villiers et al. ³⁹; Ferreira et al. ⁴⁰; McKinney ⁴¹; Hawley & Krolik ⁴²; Komissarov et al. ⁴³, Barkov & Komissarov ⁴⁴). At present, due to the apparent correlation between accretion and jet activity (e.g. Fender et al. ³), a widely accepted scenario is one in which jets are powered by accretion. The accreted matter starts to move following ordered magnetic field lines that thread the inner regions of the accretion disk. By magneto-centrifugal forces, the plasma is ejected by these magnetic field lines from the accretion disk in the direction perpendicular to it. The differential rotation of the accretion disk would create a spiral-like shape of the magnetic lines. This magnetic field configuration would accelerate and collimate the plasma. Although it is unclear at which scales the jet is already formed, VLBI observations of extragalactic jets show evidences that the collimation region could be located at $\sim 100\text{--}1000 R_{\text{Sch}}$ (e.g. Junor et al. ⁴⁵; Horiuchi et al. ⁴⁶)^b.

Once the microquasar jet is formed, it may interact with dense material ejected by the accretion disk or the stellar companion, the latter being almost unavoidable in high-mass systems. Although the role of an accretion disk wind could be to give further collimation and stability to the jet (e.g. Hardee & Hughes ⁴⁸; Tsinganos et al. ⁴⁹), the role of a strong lateral stellar wind may lead to jet bending and even disruption (Perucho & Bosch-Ramon ⁵⁰). In any case, jet/environment interaction can lead to shock formation and the radiative counterpart may be observable either as a transient phenomena, when the jet (or a discrete ejection) penetrates for the first time the surrounding medium, or as a (quasi) steady one, when the jet formation is continuous at the relevant timescales and recollimation shocks occur (Perucho & Bosch-Ramon ⁵⁰).

Despite the environment of microquasars at large spatial scales may be quite different depending on the Galaxy region or the strength of the companion star wind, the jets should stop somewhere, terminating either via disruption, in a similar way to extragalactic Fanaroff-Riley I sources (e.g. Fanaroff & Riley ⁵¹; Perucho & Martí ⁵²), or via strong shocks in the ISM, as seems to be the case for Fanaroff-Riley II sources (e.g. Fanaroff & Riley ⁵¹; Kaiser & Alexander ⁵³; Scheck et al. ⁵⁴). In either case, the radiative outcomes would be different. A classical example of the interaction between a microquasar jet and its environment at large scales is the case of the W 50-SS 433 system (e.g. Zealey et al. ⁵⁵; Velázquez & Raga ⁵⁶).

In the following sections, we list several non-thermal processes, i.e. particle acceleration and radiation, that may occur in the jet giving a (non exhaustive) overview on the literature. For the sake of clarity, we have divided the jet in several regions.

^bThe jets of the microquasar SS 433 present collimation distances, inferred from X-ray observations, apparently larger, of about $\sim 10^6 R_{\text{Sch}}$ (Namiki et al. ⁴⁷). We note however that the jet of SS 433 is quite different from a typical compact microquasar jet because of its huge kinetic power, messy environment, and thermal emitting nature.

The jet base, close to the compact object ($\sim 100 - 1000 R_{\text{Sch}}$), a region farther out, at the binary system scales (typically $\sim 10^{11} - 10^{13}$ cm), well outside the binary system -jet middle scales- (around $10^{15} - 10^{16}$ cm), and the termination regions of the jet, where it ends interacting somehow with the ISM ($\geq 10^{17}$ cm). We show in Fig. 2 a sketch of the different considered regions. Later on, with the most recent observational findings at hand, we will go deeper in the modeling to find out which of the different considered scenarios is the most suitable to explain the data.

3.3. Particle acceleration

Particle acceleration processes in microquasar jets can be of different types. At the base, the jet could be magnetically dominated (e.g., in extragalactic jets: Sikora et al. ⁵⁷), and a mechanism of particle acceleration may be magnetic energy dissipation via MHD instabilities in the jet base (e.g. Zenitani et al. ⁵⁸). Also, if jet velocities were high enough in the base, the dense available photon (from an accretion disk/corona) and matter fields could allow the converter mechanism to take place (e.g. Derishev et al. ⁵⁹; Stern & Poutanen ⁶⁰). Magnetic field reconnection in the surrounding corona could inject a non-thermal population of particles in the jet as well (e.g. Gierlinski & Done ⁶¹ and references therein). A magneto-centrifugal mechanism could also operate very close to a rotating black-hole (e.g. Neronov & Aharonian ⁶²; Rieger & Aharonian ⁶³).

At binary system scales, plausible mechanisms to generate relativistic particles in the jet are the different versions of the Fermi process: shock diffusive (Fermi I); random scattering (Fermi II); and shear acceleration (e.g. Drury ⁶⁴; Fermi ⁶⁵; and Rieger & Duffy ⁶⁶, respectively; see also Rieger et al. ⁶⁷). Fermi I mechanism could take place due to internal shocks in the jet; Fermi II acceleration could take place if magnetic turbulence is strong enough, with high Alfvén velocity; shear layer would be a natural outcome of an expanding jet or different jet/medium velocities.

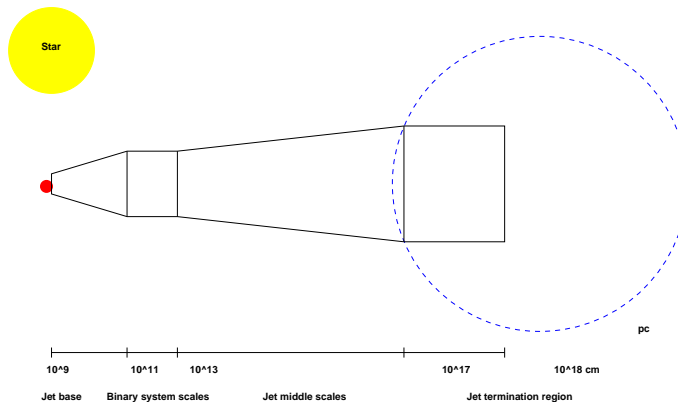


Fig. 2. Sketch of a microquasar with the different relevant scales resumed in this section.

Interactions with the stellar wind may also trigger particle acceleration via, e.g., a recollimation shock formed in the jet that expands against the dense material expelled by the companion star (e.g. Perucho & Bosch-Ramon⁵⁰). The velocities of the shocks mentioned here could be either mildly or strongly relativistic. In the latter case, the converter mechanism may be effective in very bright star systems.

At microquasar jet middle scales, some sort of shock acceleration might still take place. For instance, intermittent ejections at timescales of \sim hours–days and different velocities could create shocks at distances of about $\sim 10^{15} - 10^{16}$ cm. Also Fermi II type and shear acceleration appear plausible for a continuous outflow at these scales (something similar could happen in the intra-knot regions of extragalactic jets, see, e.g., Rieger et al.⁶⁷). Regarding the environment dynamical influence on the jet, it is not expected to be significant given the high jet ram pressure compared with the medium one at these scales.

At the microquasar jet termination point, as in AGN hot spots and radio lobes (e.g. Kaiser & Alexander⁵³), the external medium plays an important dynamical role. When the swept ISM inertia starts to affect the jet advance, two shocks may be formed, one moving backwards in the jet, the so-called reverse shock, and another one moving forward, the so-called forward or bow shock. Under these conditions, Fermi I type acceleration mechanism seems the most reasonable option, although high diffusive and convective rates in the downstream regions of the forward/reverse shocks could prevent efficient acceleration to occur. It might be the case as well that hydrodynamical instabilities distorted the jet and mixed jet matter with the ISM without forming strong shocks (e.g. Heinz & Sunyaev⁶⁸).

3.4. Radiative processes

In the jet base, depending on the dominant conditions, the relevant leptonic radiative mechanisms could be synchrotron emission (e.g. Markoff et al.⁶⁹), relativistic Bremsstrahlung from electrons interacting with jet ions (Bosch-Ramon et al.⁷⁰), SSC (e.g. Bosch-Ramon & Paredes⁷¹) and IC with corona and/or disk photons (e.g. Romero et al.⁷²; Georganopoulos et al.⁷³). Regarding hadronic processes, there are several radiative mechanisms that could produce gamma-rays, neutrinos and, as a by-product, low energy emission from secondary pairs. Two of these mechanisms are the collisions of relativistic protons with ions (pp) in the jet, and interactions between jet relativistic protons and X-ray photons (photo-meson) from the disk, the corona or the jet itself (e.g. Levinson et al.⁷⁴; Aharonian et al.⁷⁵; Romero & Vila⁷⁶ -who also account for proton synchrotron emission-). These relativistic proton collisions with ions and photons would produce neutral pions (π^0) that decay to gamma-rays, and charged pions (π^\pm) that decay to muons and neutrinos, the former decaying then to electron-positron pairs and neutrinos. Another possible hadronic mechanism is photo-disintegration, which requires the presence of UHE heavy nuclei and a dense field of target photons of large enough energy. This process produces lower mass hadrons and gamma-rays.

At binary system scales, possible radiative leptonic processes taking place in microquasars are synchrotron emission (e.g. Yuan et al. ⁷⁷; Paredes et al. ⁷⁸), relativistic Bremsstrahlung (e.g. Bosch-Ramon et al. ⁷⁰), SSC (e.g. Atoyan & Aharonian ⁷⁹; Dermer et al. ⁸⁰), and external IC (e.g. Paredes et al. ^{14,81}; Kaufman Bernadó et al. ⁸²; Georganopoulos et al. ⁷³; Dermer et al. ⁸⁰; Khangulyan et al. ⁸³). At these spatial scales, jet proton collisions with target nuclei of the stellar wind (e.g. Romero et al. ⁸⁴; Aharonian et al. ⁷⁵) seem to be the most efficient hadronic process. As noted above, this mechanism would lead as well to neutrino production (e.g. Romero et al. ⁸⁵; Aharonian et al. ⁷⁵). Other hadronic processes, which were also discussed in the literature, are photo-meson production (e.g. Aharonian ⁸⁶) and photo-disintegration (e.g. Bednarek ⁸⁷).

The emission at larger scales are commonly characterized by synchrotron radiation. At higher energies, stellar IC scattering is quite inefficient because the large distances to the companion star and the subsequent dilution of the stellar photon field. Nevertheless, for powerful ejections, SSC could still be significant (e.g. Atoyan & Aharonian ⁷⁹). Regarding the particle energy distribution, its evolution is likely dominated by convective and adiabatic energy losses (van der Laan ⁸⁸). At the termination of the jet, in case particle acceleration and confinement were efficient, synchrotron, relativistic Bremsstrahlung and IC radiation could be produced and even detected for galactic sources (e.g. Aharonian & Atoyan ⁸⁹; Bordas et al. ⁹⁰). Hadronic acceleration could take place as well, which could lead to gamma-ray production (e.g. Heinz & Sunyaev ⁶⁸) and secondary leptonic emission (e.g. Bosch-Ramon et al. ¹¹⁹).

Regarding the variability of the emission discussed above, several factors are relevant: injection could change via variations in the accelerator (e.g. injection power, injection spectrum); the target densities could vary via changes in the magnetic, photon and matter fields; geometry changes, due to e.g. orbital motion or jet precession, could affect anisotropic gamma-gamma absorption and IC scattering or the level of radiation Doppler boosting. Thus, the timescales of the variability could be linked to the injection mechanism, the radiative cooling, particle escape, and the orbital motion, depending on which mechanism plays a major role. Depending on the emitter location and size, some kinds of variability will not play a role because they will be smeared out. We come back to this issue for a more detailed discussion in Sect. 4.

3.5. Photon-photon absorption and electromagnetic cascades

Close to the compact object, either in the inner accretion disk, in the corona-like region, or in the jet base, quite extreme conditions should be present. Magnetic fields are likely high, and the same applies to the present photon fields, which may be dominated by thermal radiation from accretion peaking at UV/X-rays. Dense UV/X-ray photon fields imply that \sim GeV gamma-ray absorption close to the compact object will be very high. The strong magnetic field may suppress efficient

electromagnetic cascading, although the occurrence of cascades (e.g. Akharonian et al. ⁹²) cannot be discarded. At binary system scales, the photon-photon opacities of the stellar photon field for gamma-rays are high in massive systems. Although high-mass stars can have quite large magnetic fields in their surfaces, up to 10^3 G for a young O star (e.g. Donati et al. ⁹³), electromagnetic cascades may still develop in the system since the magnetic field strength at several stellar radii is not well known. Several authors have studied the photon-photon absorption effects in the VHE lightcurve (e.g. Protheroe & Stanev ⁹⁴; Moskalenko & Karakula ⁹⁵; Bednarek ⁹⁶; Boettcher & Dermer ⁹⁷; Dubus ⁹⁹; Khangulyan et al. ⁸³; Reynoso et al. ¹⁰⁰). The effects of absorption on the radiation variability are important not only because the photon column density changes along the orbit, but also due to the angular dependence of the cross section and the low-energy threshold of the pair creation process. The interaction angle between gamma-rays and stellar photons changes with the orbital phase. Several studies have been done in the recent years studying the impact of cascading in the gamma-ray spectrum of microquasars. Some authors have assumed that particles get deflected after creation, using a three-dimensional code to compute cascading, (e.g. Bednarek ¹⁰¹), whereas others have computed one-dimensional cascades in the direction to the observer (e.g. Aharonian et al. ⁷⁵; Orellana et al. ¹⁰²; Khangulyan et al. ⁸³). In case the magnetic field is high enough, synchrotron secondary radiation produced in the system will be significant in the radio and X-ray domains (e.g. Khangulyan et al. ⁸³; Bosch-Ramon et al. ¹⁰³). In the next section, we discuss further this issue.

4. Theoretical interpretation of observations

To interpret observations, one can use some analogies comparing one specific object with the general properties of a population of sources. Unfortunately, neither our knowledge on the physics of microquasars emitting at TeV, nor the number of these sources, are sufficient to follow this strategy. Another approach, which seems to us more suitable to study the complexity of the behavior of these objects at very high energies, is to start from basic physical processes to understand the observations in a rough but sound way. It implies to check, with the help of data and the available knowledge on each particular source, which are the most reasonable physical conditions, and processes, that lead to the observed VHE emission. To perform such an analysis, it is required to constrain the conditions in which particle acceleration is possible up to the observed energies, to know which mechanism is behind gamma-ray production (either leptonic -IC- or hadronic -pp, $p\gamma$ and nuclei disintegration-), and the impact of photon-photon absorption (and the subsequent energy release channel -synchrotron or IC-). In addition, it is important to explore the impact of particle transport (advection, diffusion or particle escape) on the final spectrum. In the following, each one of these elements is considered individually. It is worth to remark that in reality the mentioned processes will be likely coupled, and a very complex outcome can be expected, as shown in Sects. 4.2.1, 4.3.1 and 4.3.2, when

12 *V. Bosch-Ramon & D. Khangulyan*

focusing in the leptonic scenario.

4.1. *Non-thermal processes*

In this section, we explore those processes that are relevant to understand the non-thermal emission produced at very high energies for the expected conditions given in microquasars. We do not focus particularly in the jet but also in its environment. In particular, we consider particle acceleration, particle energy losses and transport, and photon-photon absorption and electromagnetic cascading.

4.1.1. *Particle acceleration*

Our aim is not to model accurately what is observed, but to derive basic and solid constraints from the available data. The first step is to set a necessary condition for acceleration of a charged particle of a certain energy to occur, which is given by the Hillas criterium (Hillas ¹⁰⁴). This consists on the fact that particles can only be accelerated if their Larmor radius ($r_L = E/qB_a$; where B_a is the accelerator magnetic field, and q and E are the charge and energy of the particle, respectively) is smaller than the accelerator size (l_a), since otherwise they will escape the accelerator. This limits the highest achievable energy to:

$$E < qB_a l_a, \quad (1)$$

which can be rewritten in the following form:

$$E < 30 \frac{q}{e} B_{a,G} l_{11} \text{ TeV}, \quad (2)$$

where e is the electron charge, $B_{a,G}$ is the accelerator magnetic field (B_a) in Gauss units, and $l_{11} = l_a/10^{11}$ cm. Nevertheless, to determine whether particles can be accelerated up to a certain energy, the specific acceleration and energy loss (or particle escape) mechanisms are to be known: $t_{\text{acc}} = t_{\text{cool/esc}}$. In general, the acceleration timescale can be expressed as:

$$t_{\text{acc}} = \eta \frac{r_L}{c} \simeq 0.1 \eta \frac{e}{q} E_{\text{TeV}} B_{a,G}^{-1} \text{ s}, \quad (3)$$

where η is a dimensionless phenomenological parameter (or function) representing the acceleration efficiency, and E_{TeV} is the particle energy in TeV units. The particular case of $\eta = 1$ corresponds to the shortest possible acceleration time independently of the acceleration mechanism. Another instance for η can be given for the case of non-relativistic diffusive shock acceleration (plane shock with weak magnetic field, in the test particle approximation) (e.g. Protheroe ¹⁰⁵):

$$\eta = 2\pi \frac{D}{D_{\text{Bohm}}} \left(\frac{c}{v_{\text{sh}}} \right)^2, \quad (4)$$

where v_{sh} is the shock velocity, and D is the diffusion coefficient (D_{Bohm} in the Bohm limit). For $v_{\text{sh}} = 3 \times 10^9 \text{ cm s}^{-1}$ and $D = D_{\text{Bohm}}$, $\eta \sim 10^3$.

As an example of the importance of using acceleration constraints, we show in Fig. 3 a 2-dimensional $d_a - B_a$ map for a compact high-mass microquasar with stellar luminosity $L_* = 10^{39}$ erg s $^{-1}$, $d_* = 3 \times 10^{12}$ cm and $kT_* \approx 3$ eV. d_a is the distance from the accelerator to the star. As done by Khangulyan et al. ⁸³, it is possible to restrict d_a and η . In the case of LS 5039, for instance, for reasonable $\eta \geq 10$, and the detected 30 TeV photon energies, the accelerator should be outside the system, i.e. $d_a > 2 \times 10^{12}$ cm.

Particle transport

Without focusing on any particular acceleration mechanism, we note that, either the maximum energy is limited by cooling, which implies that particles radiate most of their energy before escaping the accelerator, or their escape stops acceleration. In the latter case, the emitter itself can be considered larger than the acceleration region. The escape time (t_{esc}) can be characterized, in the accelerator as well as in the whole emitter, by the minimum among the diffusion (t_{diff}) and the advection (t_{adv}) times:

$$t_{\text{esc}} = \min(t_{\text{diff}}, t_{\text{adv}}), \quad (5)$$

which can be expressed either as:

$$t_{\text{diff}} = \frac{l^2}{2D(E)} \sim 2 \times 10^4 l_{12}^2 \left(\frac{D_{\text{Bohm}}}{D(E)} \right) B_G E_{\text{TeV}}^{-1} \text{ s}, \quad (6)$$

for 1-dimensional diffusion in the accelerator/emitter, where l ($l_{12} = l/10^{12}$ cm) is the (accelerator/emitter) size covered by diffusion, and B_G is the emitter magnetic

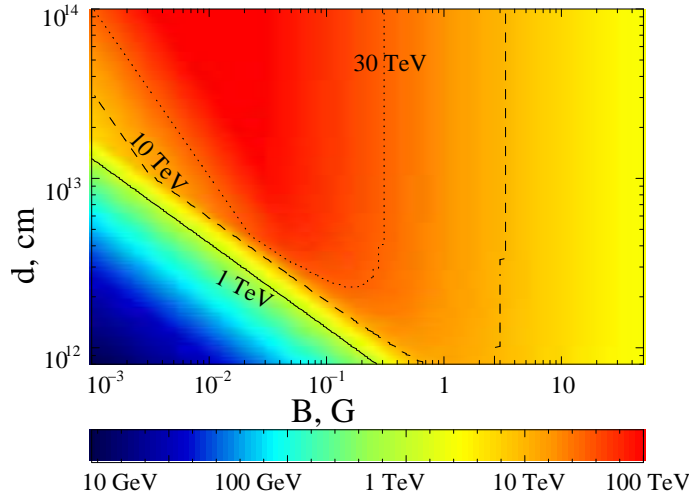


Fig. 3. 2-dimensional $d - B$ map that shows the maximum achievable energy for $\eta = 10$ for different d_a and B_a values. The adopted parameter values are $L_* = 10^{39}$ erg s $^{-1}$, $d_* = 3 \times 10^{12}$ cm and $kT_* \approx 3$ eV.

14 *V. Bosch-Ramon & D. Khangulyan*

field; or as:

$$t_{\text{adv}} = \frac{l}{V_{\text{adv}}} \sim 10^4 l_{12} V_8^{-1} \text{ s}, \quad (7)$$

for advection, where V_{adv} is the advection speed ($V_8 = V_{\text{adv}}/10^8 \text{ cm s}^{-1}$).

Under the impact of cooling, the typical distance up to which particles can propagate is:

$$l_{\text{diff}} = 10^{10} E_{\text{TeV}}^{1/2} B_G^{-1/2} t_{\text{cool}}^{1/2} \left(\frac{D}{D_{\text{Bohm}}} \right)^{1/2} \text{ cm}, \quad (8)$$

under diffusive transport, and:

$$l_{\text{adv}} = 10^{10} \left(\frac{V_{\text{adv}}}{10^{10} \text{ cm/s}} \right) t_{\text{cool}} \text{ cm}, \quad (9)$$

under advective transport. t_{cool} is the cooling timescale (in s) of the dominant loss mechanism. We discuss in the following different cooling processes that may be relevant in the microquasar context.

4.1.2. Radiative processes

Synchrotron

In the presence of a disordered magnetic field, electrons radiate via synchrotron emission. The synchrotron cooling timescale is approximately:

$$t_{\text{sy}} \approx 4 \times 10^2 \left(\frac{e}{q} \right)^4 (m/m_e)^4 B_{\text{a,G}}^{-2} E_{\text{TeV}}^{-1} \text{ s}, \quad (10)$$

where m and m_e are the mass of the particle and the electron, respectively. This gives the maximum particle energy:

$$E_{\text{max}} \approx 60 \left(\frac{e}{q} \right)^{3/2} (m/m_e)^2 (\eta B_{\text{a,G}})^{-1/2} \text{ TeV}. \quad (11)$$

This process is only relevant for leptons unless the magnetic field is very strong, in which case hadronic synchrotron may become efficient.

To see what may happen in a microquasar regarding E_{max} under synchrotron cooling, we take $B_{0,G} = 10^6 \text{ G}$ as a reasonable value for the jet base magnetic field (at $\sim 50 R_{\text{Sch}} \sim 10^8 \text{ cm}$ from the compact object), obtaining: $E_{\text{max}} \approx 0.06 \eta^{-1/2} \text{ TeV}$. If we assume a distance dependence of B of the form $1/Z$ and locate the accelerator at 10^{12} cm , we obtain: $E_{\text{max}} \approx 6 \eta^{-1/2} \text{ TeV}$, i.e. in such a situation, it seems unlikely to produce VHE leptons in the jet even at the system scales.

At spatial scales similar or smaller than the binary system, it seems reasonable to expect large magnetic fields related either to the jet, to the accretion disk, or to the companion star. It implies that synchrotron emission can be an efficient radiation process, and electrons may release most of their energy via synchrotron emission.

At larger scales, if no significant magnetic field enhancement takes place, efficiencies will decrease strongly.

It is worthy using Eqs. (8) and (9) to calculate the impact of synchrotron losses on the propagation of electrons via diffusion and advection, since they tell how far relativistic electrons can go without assuming additional acceleration and neglecting other sources of losses. Under the next parameter choice, e.g. $B \sim 1$ G, $V_{\text{adv}} = 10^{10}$ cm s $^{-1}$, $D = D_{\text{Bohm}}$, advection is the most effective transport mechanism, and TeV particles may reach distances of $\sim 3 \times 10^{12}$ cm from their injection point.

Inverse Compton

Under the radiation field of the primary star in a high-mass microquasar, or in the case of strong accretion disk/corona emission, IC scattering is to be considered and may limit particle acceleration. Synchrotron self-Compton could become a dominant process, although it is not treated here, since it would require significantly large magnetic fields, making acceleration up to very high energies unlikely due to strong synchrotron/Thomson IC energy losses. In addition, once the electron enters in the KN IC regime, the interaction efficiency reduces strongly and synchrotron cooling becomes dominant, making SSC not very efficient in the TeV range under UV photon fields. We note that, due to the same reason as in the synchrotron case, IC losses are only significant for leptons^c.

For a Planckian distribution of target photons with temperature T , the IC energy loss rate can be approximated, with an accuracy of less than a 3%, by:

$$\dot{\gamma}_{IC} = 5.5 \times 10^{17} T_{\text{mcc}}^3 \gamma \frac{\ln(1 + 0.55\gamma T_{\text{mcc}})}{1 + 25T_{\text{mcc}}\gamma} \left(1 + \frac{1.4\gamma T_{\text{mcc}}}{1 + 12\gamma^2 T_{\text{mcc}}^2} \right) \text{ s}^{-1}, \quad (12)$$

where $T_{\text{mcc}} = kT/m_e c^2$.

Regarding the particle maximum achievable energy, at the energies in which we are interested in this work, IC scattering proceeds in the Klein-Nishina (KN) regime ($\gamma \gg 1/kT$ in $m_e c^2$ units). In such a case, a simple power-law fit for the cooling time can be used for a black-body type of target photon distribution:

$$t_{IC} \approx 10^2 \left(\frac{R}{R_*} \right)^2 T_4^{-2.3} E_{\text{TeV}}^{0.7} \text{ s}. \quad (13)$$

where R and R_* are the distance to the origin and the radius of the source of target photons, and $T_4 = T_*/10^4$ K. Eq. (13) can be expressed in a more convenient form in case of a hot and massive primary star as the dominant source of target photons:

$$t_{IC} = 10^2 (w_{100})^{-1} \left(\frac{T_*}{3 \times 10^4 \text{ K}} \right)^{1.7} E_{\text{TeV}}^{0.7} \text{ s}, \quad (14)$$

where $w = 100 w_{100}$ erg cm $^{-3}$ is the target photon field energy density, and T_* the stellar temperature. This expression gives a reasonable agreement for the IC cooling

^cFor hadrons, other cooling processes, mainly photo-meson production, discussed further in the text, will overcome hadronic IC scattering.

16 *V. Bosch-Ramon & D. Khangulyan*

time, within a factor ≤ 2 , in the relevant energy range:

$$0.1 \text{ TeV} \left(\frac{T_{\text{star}}}{3 \times 10^4 \text{K}} \right)^{-1} < E < 3 \times 10^3 \text{ TeV} \left(\frac{T_{\text{star}}}{3 \times 10^4 \text{K}} \right)^{-1}. \quad (15)$$

The corresponding value of the maximum energy is:

$$E_{\text{max}} \approx 4 \times 10^{10} [B_{\text{a G}} \eta^{-1} w_{100}^{-1}]^{3.3} \text{ TeV}, \quad (16)$$

which shows that KN IC limits particle acceleration much less than synchrotron radiation, and can be hardly dominant at the maximum particle energy for reasonable magnetic fields in any region of the microquasar.

To estimate the impact of IC losses on the propagation of electrons via diffusion and advection, Eqs. (8) and (9) can be used as well. Like in the case of synchrotron losses, for the conditions $B \sim 1 \text{ G}$, $V_{\text{adv}} = 10^{10} \text{ cm s}^{-1}$ and $D = D_{\text{Bohm}}$, and IC loss dominance, advection is again the most efficient transport mechanism, under which TeV particles could reach distances up to $\sim 10^{12} \text{ cm}$.

Proton-proton interactions

As mentioned in the previous section, purely hadronic processes like pp interactions have been discussed in the past in the context of microquasars. We consider them here as well, since they may be relevant in some cases. The energy loss timescale for pp collisions (Kelner et al. ¹⁰⁶) is:

$$t_{\text{pp}} \approx \frac{10^6}{n_9} \text{ s}, \quad (17)$$

where $n_9 = n_t/10^9 \text{ cm}^{-3}$ is the target density. The energy threshold of this process in the reference frame of the interaction center of masses is the pion rest mass, $\approx 140 \text{ MeV}$. From Eqs. (18) and (17), the maximum particle energy can be derived:

$$E_{\text{max}} \approx 10^7 \frac{B_{\text{a,G}}}{\eta n_9} \text{ TeV}. \quad (18)$$

Given the long cooling timescale, the maximum energy will be likely limited by the accelerator size.

Defining L_p as the luminosity injected in the form of relativistic protons, the luminosities in gamma-rays, neutrinos and secondary electron-positron pairs are, with differences of about a factor of 2 (Kelner et al. ¹⁰⁶), the next ones:

$$L_\gamma \approx \min(1, t_{\text{esc}}/t_{\text{pp}}) c_{\text{pp}} L_p, \quad (19)$$

where c_{pp} is the energy transfer efficiency from relativistic protons to secondary particles ($\sim 10\%$). In the context of high-mass microquasars, a reasonable lower limit for t_{esc} is the wind advection time, i.e. the time required for the stellar wind to cross the orbital radius (R_{orb}/V_w ; where $R_{\text{orb}} \sim 10^{12} - 10^{13} \text{ cm}$ and $V_w \sim 1 - 3 \times 10^8 \text{ cm s}^{-1}$), $t_{\text{esc}} \leq 10^4 \text{ s}$; and a very lower limit is set by the speed of light, i.e. $t_{\text{esc}} \geq 10^2 \text{ s}$. All this, plus adopting a $\dot{M} = 10^{-6} M_\odot \text{ yr}^{-1}$ (typical for O stars), yields:

$$L_\gamma \sim 10^{-5} - 10^{-3} L_p.$$

Larger efficiencies cannot be discarded in some specific cases, like density enhancements in the wind or even in the jet itself via, e.g., shocks. Once relativistic protons leave the binary system, the expected density decreases in the stellar wind as well as in the jet, making pp collisions negligible.

Photo-meson production

Among different hadronic processes, photo-meson production (Kelner et al. 107) is worthy also to be considered. The energy threshold for this process is:

$$E_{\text{th } p\gamma} = m_p c^2 \epsilon_{\text{th } p\gamma} / 2\epsilon = (5 \times 10^4 \text{ TeV}) (T_4)^{-1}, \quad (20)$$

where m_p is the proton mass and ϵ and $\epsilon_{\text{th } p\gamma} \approx 140 \text{ MeV}$ are the energy of the target photon in the laboratory and the hadron rest frames, respectively. The loss rate is given by:

$$t_{p\gamma} \sim \frac{10^{18}}{N_X} \text{ s}, \quad (21)$$

where:

$$N_X \approx \frac{L}{4\pi\epsilon R^2 c} \approx 2 \times 10^{14} L_{38} T_4^{-1} R_{12}^{-2} \text{ cm}^{-3}. \quad (22)$$

L_{38} is the star luminosity $L_*/10^{38} \text{ erg s}^{-1}$, R_{12} is the distance to the star, and $R/10^{12} \text{ cm}$. Eq. (21) can be rewritten as:

$$t_{p\gamma} \sim 10^4 L_{38}^{-1} T_4 R_{12}^2 \text{ s}. \quad (23)$$

With this cooling timescale, the corresponding maximum energy is:

$$E_{\text{max}} \sim 10^5 \eta^{-1} B_{a,G} L_{38}^{-1} T_4 R_{12}^2 \text{ TeV}. \quad (24)$$

As for pp interactions, the long cooling timescales of photo-meson production imply that the maximum energy is in fact limited by the accelerator size. We note that only in case a substantial part of the energy in accelerated protons were $> E_{\text{th } p\gamma} \sim 10^4 \text{ TeV}$, under an UV photon field, and the fastest protons escaped at the speed of light, photo-meson production could reach efficiencies of $L_\gamma \sim 10^{-3} L_p^{\text{d}}$ for $E_p > E_{>\text{th } p\gamma}$. The energy transfer efficiency for this process is $c_{p\gamma} = 0.1$. In the inner regions of the jet, close to the accretion disk and corona photon fields, the radiation energy density may be high enough to get even higher efficiencies. The larger target photon energy would imply a reduced threshold energy. Nevertheless, the constraint imposed by Eq. (2) is quite restrictive and could prevent hadrons from reaching energies $> E_{\text{th } p\gamma}$ for reasonable B_a and l_a values. Namely, comparing Eqs. (24), (20) and (2), two conditions are obtained:

$$B_G T_4 l_{11} > 2 \times 10^3, \quad (25)$$

for basic physical conditions; and

$$\eta < B_{a,G} T_4^2 R_{12}^2 / 2 L_{38}. \quad (26)$$

^dAt the involved proton energies, the stellar wind can hardly confine the particles, thereby we adopt the speed of light as escape velocity.

for the acceleration efficiency.

As in the case of pp collisions, the strong dilution of the photon field far from its source prevents photo-meson production from being efficient outside the binary system.

Photo-disintegration

If ultra relativistic heavy nuclei are present, they can suffer photon disintegration under the ambient photon field. The expression for the threshold energy is similar to that presented in Eq. (20):

$$E_{\text{th pd}} = m_N c^2 \epsilon_{\text{th pd}} / 2\epsilon, \quad (27)$$

where m_N is the mass of the nucleus and $\epsilon_{\text{th pd}} = 8$ MeV. Effectively, since m_N can be up to $\sim 100 m_p$, $E_{\text{th pd}}$ could be $> E_{\text{th p}\gamma}$.

The disintegration of the nuclei has as typical timescale:

$$t_{\text{pd}} \sim 10^3 L_{38}^{-1} T_4 R_{12}^2 \text{ s}. \quad (28)$$

For simplicity, we have assumed that the mass of the nucleus is its charge times the mass of the proton, which slightly overestimates the efficiency within a factor of ~ 2 . In addition, a slow dependence on the mass of the nuclei in the cross section has been neglected. Photo-disintegration would stop the acceleration of heavy nuclei at energies:

$$E_{\text{max}} \sim 10^4 \frac{q}{e} B_{\text{a,G}} L_{38}^{-1} T_4 R_{12}^2 \text{ TeV}. \quad (29)$$

As in the case of pp collisions and photo-meson production, the accelerator size instead of photo-disintegration cooling will probably stop acceleration of heavy nuclei. Taking into account that the energy transfer efficiency is $c_{\text{p}\gamma} \sim 0.01$, and adopting the speed of light to derive a lower-limit for t_{esc} , photo-disintegration can yield in gamma-rays $L_\gamma \sim 10^{-3} L_N$, where L_N is the energy stored in heavy nuclei with $E > E_{\text{th pd}}$. Hillas constraint allows energies m_N/m_p times larger for nuclei than for protons, although as noted above $E_{\text{th pd}}$ can be $> E_{\text{th p}\gamma}$ ^e. Like in the case of photo-meson production, it is unclear whether enough energy can be in the form of ultra relativistic heavy nuclei above the threshold to produce a significant signal via photo-disintegration.

Photon-photon absorption and secondary radiation

The presence of the star, a powerful source of UV photons, is very relevant to understand TeV emission from compact sources. A massive and hot star is an excellent provider of target photons for photon-photon absorption. The anisotropy of the stellar photon field and the relative position of the system with respect to the observer makes the exploration of the observational impact of photon-photon absorption a non-trivial subject. In Fig. 4, we show a 2-dimensional map of the opacity coefficient (τ) for different energies of the incoming photon (E_γ) emitted

^eActually, similar constraints to those derived for photo-meson production regarding the interaction physical conditions and the acceleration efficiency apply here as well.

near the compact object, and different directions starting with the one pointing away from the star. Here, θ is the angle with the line joining the TeV emitter and the star. The point-like approximation for the target photon field has been used, which implies that $\tau \propto 1/d$. The used parameter values are $L_* = 10^{39}$ erg s $^{-1}$, $d_* = 3 \times 10^{12}$ cm and $kT_* = 3$ eV. It is worthy noting that the point-like approximation for the target photon emitter works in a wide range of situations, but there are cases relevant for compact TeV sources in which is necessary to account for the finite size of the star (see also Dubus⁹⁹). In Fig. 5, we show a 2-dimensional map of the ratio τ_p/τ_f (i.e. point-like versus finite size τ) for different distances to the star (d) and values of θ . The radius of the star has been taken $R_* = 7 \times 10^{11}$ cm. The energy of the incoming photon has been taken 1 TeV. The deep blue/black regions in this map represent the cases when the point-like approximation gives almost no absorption, i.e. when the emitter points roughly away from the star, or when the photons in the finite size approximation collide with the star surface giving infinite opacity.

The importance of cascading has been already stated above. It is worth now to study the possibility of cascade development in the surroundings of massive and hot stars. There are two extreme situations. Either the magnetic field energy density is much lower compared with the radiation energy density, and in such a case pure cascade will develop, or the magnetic field energy density is a significant fraction, or above, the radiation one, and then the electron energy will be mostly released via synchrotron radiation and single-scattering IC. If the magnetic field is low enough (and therefore suitable for cascading to occur), very high-energy particles will be only slightly deflected before radiating their energy via IC. This allows us for a 1-dimensional approach to compute cascading. For the same parameter values as those presented above, we have performed a 1-dimensional electromagnetic cascade simulation, the result of which is shown in Fig. 6. The injected particle spectrum was a power-law of photon index 2.

To give an idea of the magnetic field importance, next formula shows the critical value of the magnetic field that allows cascading to occur for TeV electrons:

$$B_c = 10 \frac{R_*}{R} \left(\frac{L_*}{10^{39} \text{ erg s}^{-1}} \right)^{1/2} \text{ G}, \quad (30)$$

In fact, B_c is valid for the 1-dimensional cascade case. If electrons suffer strong deflection in the ambient magnetic field, the longer time required by particles to escape the region of dense photon field will increase the synchrotron outcome with respect to the IC one. This happens since photons convert to electrons more times before escaping, releasing at the end more energy in form of synchrotron and low energy IC radiation. From all this, and the fact that magnetic fields of hundreds of G are typical in the surface of OB stars, we conclude that effective electromagnetic cascading is unlikely in the environment of high-mass systems. For the same conditions as those taken for Fig. 6, plus a stellar surface magnetic field of 100 G and a primary gamma-ray injection luminosity of 3×10^{35} erg s $^{-1}$, we show the secondary pair spectral energy distribution (SED) in Fig. 7. We note the moderately high

20 *V. Bosch-Ramon & D. Khangulyan*

radio and X-ray luminosities (see also Bosch-Ramon et al. ¹⁰³).

4.2. Modeling non-thermal emission in microquasars: the case of *Cygnus X-1*

In Sect. 4.1, we have reviewed the main radiative processes that could take place under typical conditions in microquasars. After roughly estimating the efficiency of different leptonic and hadronic processes, it is our aim now to focus on the mechanism that, to our understanding, is the most likely to produce the VHE radiation observed in some of these sources. From the point of view of efficiency, IC scattering is clearly a good candidate in this sense. In addition, the fact that a hot and massive star is present in all these systems detected at TeV energies makes IC scattering very attractive^f. Finally, the pattern of variability of the spectrum and flux along the orbit found in LS 5039 can be, together with photon-photon

^f It does not discard low-mass microquasars as VHE emitters. Actually, from the observational point of view, hints of TeV emission from GRS 1915–105 were found using imaging Cherenkov techniques by HEGRA (Aharonian & Heinzlmann ¹⁰⁸) and Whipple (Rovero et al. ¹⁰⁹). In addition, a number of theoretical works have proposed these sources as VHE emitters (e.g. Atoyan & Aharonian ⁷⁹; Bosch-Ramon et al. ⁷⁰; Romero et al. ⁷⁶).

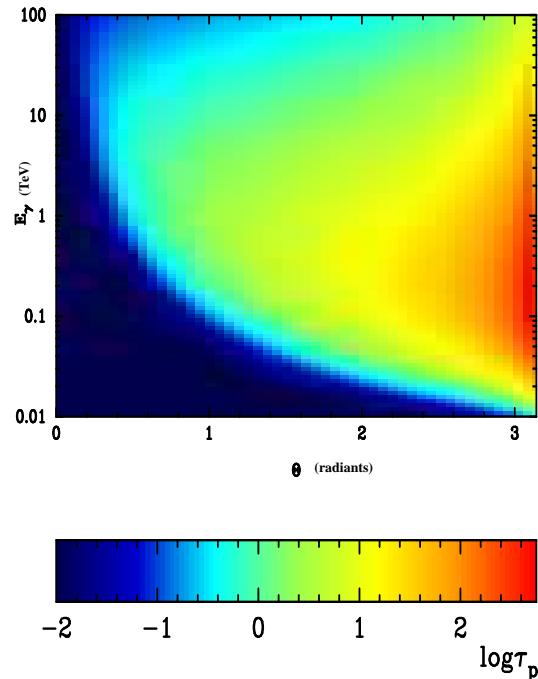


Fig. 4. 2-dimensional $\theta - E_{\text{gamma}}$ map of the opacity coefficient. The adopted parameter values are $L_* = 10^{39} \text{ erg s}^{-1}$, $d_* = 3 \times 10^{12} \text{ cm}$ and $kT_* = 3 \text{ eV}$.

absorption, explained due to the angular dependence of the cross section of IC scattering and the anisotropic nature of the stellar photon field (e.g. Khangulyan & Aharonian 110; Khangulyan et al. 83).

To carry out a simple but thorough treatment of the processes relevant to VHE emission in microquasars, we have simplified the scenario as much as possible. We show a schema of this scenario in Fig. 8. We consider the jet as a weakly relativistic convective flow without going into the details of its physical nature, i.e. whether it is a magneto- or a hydrodynamical plasma, or even a pointing flux dominated flow. This outflow is ejected perpendicular to the orbital plane bearing a disordered magnetic field attached to it. Efficient acceleration of non-thermal particles can occur at a certain location in the jet (Z_0 from the compact object, d_0 from the star); such acceleration regions are treated as point-like, and their position in the jet, Z_0 , could change. For simplicity, we adopt a model in which acceleration takes place only in one point.

Because of the strong uncertainties affecting the physics of microquasar jets, we do not treat but very generally the acceleration processes that may take place in there. The injection electron spectrum adopted here is phenomenological: a power law of exponent -2 plus an exponential high-energy cutoff. The accelerator sets up

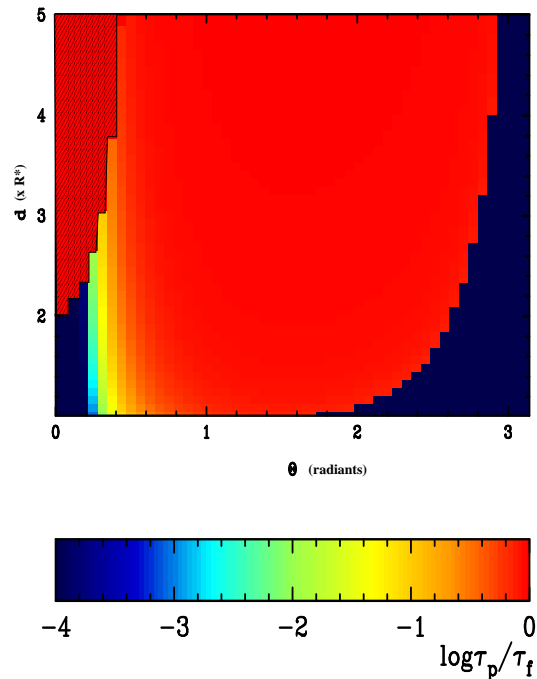


Fig. 5. 2-dimensional $\theta - d$ map of the ratio $\tau_{p-1}/\tau_{\text{fn}}$ for an incoming photon of 1 TeV. The adopted parameters are the same as those of Fig. 4, plus the stellar radius $R_* = 7 \times 10^{11}$ cm. The shaded area to the left of the plot corresponds to a region of opacities ~ 0 .

22 *V. Bosch-Ramon & D. Khangulyan*

the initial conditions of the emitter, which is treated as a 1-dimensional region where particles are transported by jet convection. Adiabatic losses have been neglected here. The magnetic field depends on Z like $B = B_a(Z_0/Z)$. To model the

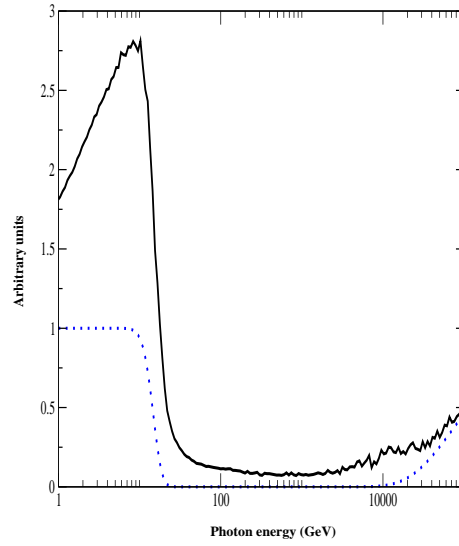


Fig. 6. 1-dimensional electromagnetic cascade. Note the difference of about a factor of 10 between the 1 TeV and the 10 GeV fluxes. The adopted parameters are those of Fig. 4.

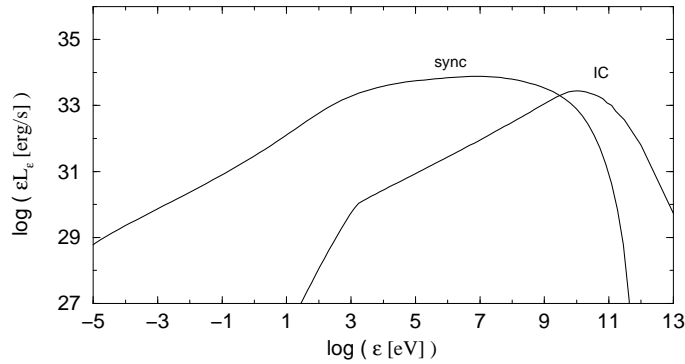


Fig. 7. Computed SED of the synchrotron and IC emission from the pairs created in a compact binary. The TeV emitter location is at $d = 3 \times 10^{12}$ cm. The adopted parameters are those of Fig. 4, plus a stellar surface magnetic field of 100 G and a primary gamma-ray injection luminosity of 3×10^{35} erg s^{-1} .

non-thermal processes included in our scenario, it is necessary to consider the presence of different ingredients: the magnetic field, possibly present radiation fields, and the material in which the emitting particles may be embedded. As discussed above, we will deal here with synchrotron and stellar IC emission, since we restrict ourselves to high mass systems and to the most relevant processes to produce or affect VHE radiation. Nevertheless, other mechanisms cannot be discarded. We take into account the impact of photon photon absorption on the VHE spectrum. We recall the importance of the geometry of IC scattering and photon photon absorption for the spectra and lightcurves when the star is the main source of target photons. For further mathematical details of the model, we refer to Khangulyan et al. ⁸³.

In the following, we apply this model to the microquasar Cygnus X-1 (Sect. 4.2.1), and to the other two X-ray binaries with extended radio emission, LS 5039 and LS I +61 303 (Sect. 4.3).

4.2.1. Application to Cygnus X-1

Cygnus X-1 is a HMXB of uncontroverted accreting nature with relativistic radio jets (Stirling et al. ¹¹¹). The compact object is a black-hole of $\sim 20 M_{\odot}$, the primary is an O9.7Iab star of $\sim 40 M_{\odot}$, and the system is located at ≈ 2.1 kpc (Ziolkowski ¹¹²). The orbit is thought to be circular, with an inclination $i \sim 30^{\circ}$, orbital radius of $\approx 3 \times 10^{12}$ cm and period of 5.6 days (Gies & Bolton ¹¹³). The primary star presents a luminosity of $\approx 10^{39}$ erg s^{-1} and a temperature of ≈ 30000 K. An

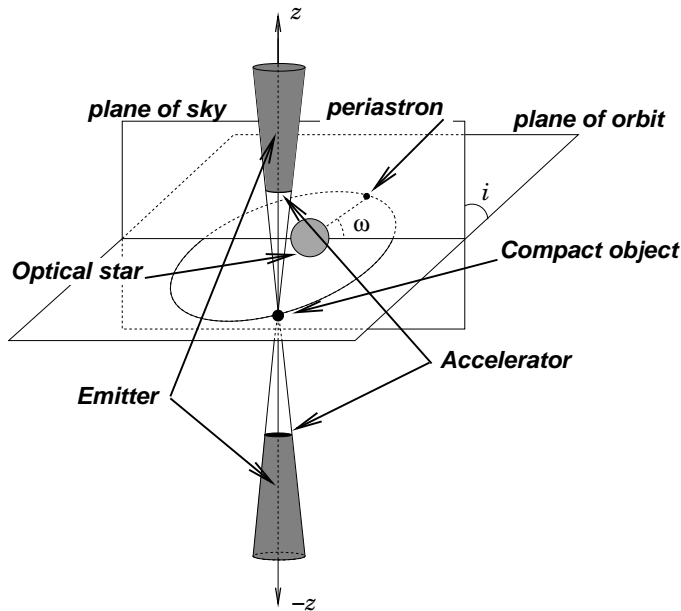


Fig. 8. Schema of the system.

evidence of detection from this source at the 4.1σ level has been found by MAGIC in the TeV range during a transient event that may be correlated with the hard X-ray behavior (Albert et al. ¹⁵). At present, the origin of the VHE emission is unclear. In the context of the hadronic scenario, Romero et al. ⁸⁴ and Orellana et al. ¹⁰² computed the emission for a microquasar with the characteristics of Cygnus X-1. Regardless the hadronic or leptonic origin of the gamma-ray radiation, electromagnetic cascading and/or secondary synchrotron emission should occur in the system (e.g. Bednarek ¹¹⁴, Orellana et al. ¹⁰², Bosch-Ramon et al. ¹⁰³).

On the spectral energy distribution and orbital variability

It is worthy to see the aspect of the multiwavelength non-thermal emission inferred from the VHE radiation detected from the source. This is shown in Fig. 9. We have located the accelerator/emitter at $Z_0 = 3 \times 10^{12}$ cm. The magnetic field is \sim G. The synchrotron X-ray flux is well below the observed level, of likely thermal (comptonized) origin (Sunyaev & Truemper ¹¹⁵). This SED has been calculated for an emitter located in the borders of the system, in which opacities are moderate. However, deeper, closer to the compact object, the attenuation factor grows orders of magnitude.

For Cygnus X-1, the spectrum of the emission from $\sim 0.1 - 1$ TeV electrons is available for a narrow orbital phase range around $\phi = 0.9$, i.e. this is not averaged for wide ranges of the orbit. In addition, these electrons have the shortest lifetimes under IC cooling, implying that they radiate most of their energy before propagating significantly. These two facts mean that the observed radiation was produced under similar conditions. In addition, the stellar photon field is very dense in the compact object surroundings, implying very large opacities in almost all the directions. All this, plus the known orbital observer/system geometry at the observation phase, allows us, and makes interesting, to estimate the absorbed energy via photon-photon absorption depending on the distance between the emitter and the compact object. The calculation of the energy processed in this system via photon-photon absorption can give a model-independent constraint on the the location of the TeV emitter.

In Fig. 10, we show the luminosity divided by $4\pi d_{\odot}^2$ (d_{\odot} : distance to the Earth) of the secondary pairs injected in the system as a function of the distance to the compact object. This is computed calculating first the deabsorbed VHE spectrum and flux given the distance to the star and the observed spectrum and flux (Albert et al. ¹⁵). In our calculations we have not taken into account the effect of cascading, although the likely moderate-to-high magnetic fields present in massive binary systems would imply a dominant synchrotron channel suppressing cascading. Since in our context a significant fraction of this energy rate is released via synchrotron emission, and the X-ray/soft gamma-ray luminosities are typically of $\sim 10^{37}$ erg s⁻¹ (e.g. McConnell et al. ¹¹⁶), the emitter location can be set, conservatively, to at least few times 10^{12} cm (see also Bosch-Ramon et al. ¹¹⁷). This is a strong indication that the TeV emitter is located in a jet far away from the compact object. It is relevant also to note that the secondary synchrotron radiation may also explain the observed soft gamma-ray fluxes (e.g. McConnell et al. ¹¹⁶). Another interesting

result is the absorbed luminosity at distances $\sim 10^{13}$ cm, indicating that there can be significant injection of relativistic pairs at distances where their radio emission may be resolved using VLBI techniques (see also Bosch-Ramon et al. ¹⁰³).

Regarding the time evolution of the observed radiation, the flaring nature of the VHE emission points to intrinsic changes of the emitter properties, instead of geometric effects or target density variations, as the origin of the variability.

4.3. TeV binaries with extended radio emission: LS 5039 and LS I +61 303

4.3.1. LS 5039

LS 5039 is an HMXB (Motch et al. ¹¹⁸) located at 2.5 ± 0.5 kpc (Casares et al. ¹⁸). The source presents radio jets (Paredes et al. ^{14,81}), shows X-ray variability possibly associated to the orbital motion (Bosch-Ramon et al. ¹¹⁹), and has been detected at very high-energy (VHE) gamma-rays (Aharonian et al. ¹⁶), which virtually confirms its association with a CGRO/EGRET source (Paredes et al. ¹⁴). Interestingly, the TeV emission varies with the orbital period (Aharonian et al. ¹⁷). The most recent orbital ephemeris of the system were obtained by Casares et al. ¹⁸. The orbital period is 3.9060 days, the eccentricity is moderate $e = 0.35 \pm 0.04$, and the inclination angle is not well constrained, $i \approx 15^\circ - 60^\circ$. The orbital semi-major axis of the system is $\approx 2 \times 10^{12}$ cm. The nature of the compact object is still uncertain. Casares et.

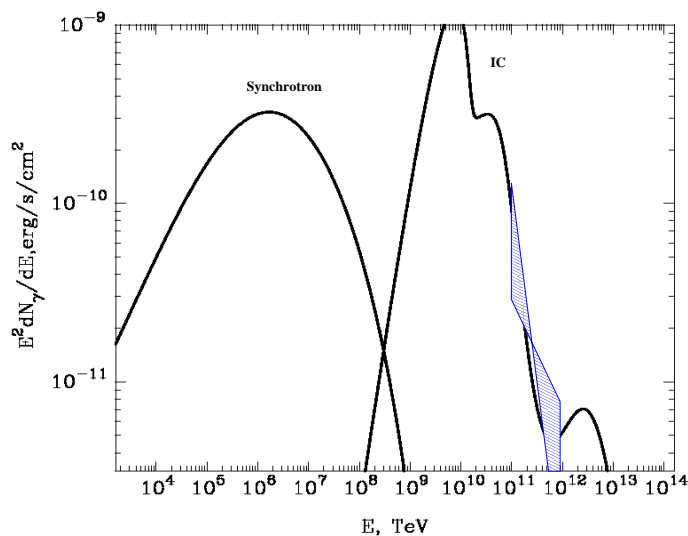


Fig. 9. Computed synchrotron and IC SED for Cygnus X-1, together with the observed VHE SED, is shown. The accelerator/emitter location has been set to $Z_0 = 3 \times 10^{12}$ cm. The total contribution from the jet and the counter-jet is shown.

al. ¹⁸ suggested that it may be a black hole[§], although there is an on-going debate on this issue, and some authors have proposed that LS 5039 is in fact a young non-accreting pulsar (see, e.g., Martocchia et al. ¹²⁰; see also Dubus ¹³⁹). In this regard, the strongest argument would be the lack of accretion features in the X-ray spectrum of LS 5039.

The radio emission in LS 5039 is of non-thermal origin, slightly variable at month–year timescales ($\sim 20\text{--}30\%$) and extended $\sim 1\text{--}100$ milliarcseconds (mas)- (Martí et al. ¹²⁴; Ribó et al. ¹²¹; Paredes et al. ^{14,81}, Ribó et al. ¹²²; for an exhaustive study of this source, see Ribó ¹²³), the $\sim 60\text{--}80\%$ being produced within a core of \sim mas. The radio emission, when observed at VLA angular resolution, appears unresolved, and optically thin (Martí et al. ¹²⁴).

In the X-rays, the source shows flux variations by a factor of ~ 2 peaking smoothly around phase 0.8 and more sharply at other phases (Bosch-Ramon et al.

[§]Assuming pseudo-synchronization of the orbit.

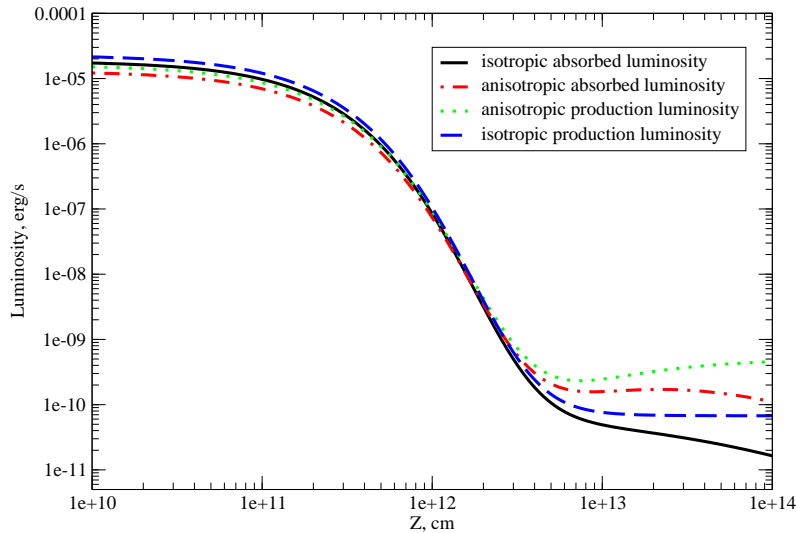


Fig. 10. Luminosity divided by $4\pi d_{\odot}^2$ of the secondary pairs injected in the system with the emitter at different distances from the compact object. This is computed calculating first the deabsorbed VHE spectrum and flux given the distance to the star and the observed spectrum and flux. The case in which the radiation process is isotropic, like proton-proton collisions may be (solid line), and the case in which the radiation process is IC (dot-dashed line) -strongly anisotropic-, are shown. The production curves for both cases are also shown.

119). These peaks were apparently accompanied by spectral hardening. At phases ~ 0.8 , higher and harder emission than in the rest of the orbit has been also observed at TeV energies (Aharonian et al. 17), and simultaneous Chandra observations have apparently shown a similar behavior in X-rays (Horns et al. 125; Bosch-Ramon et al. 126).

At VHE, the flux and the photon index change periodically, by a factor of

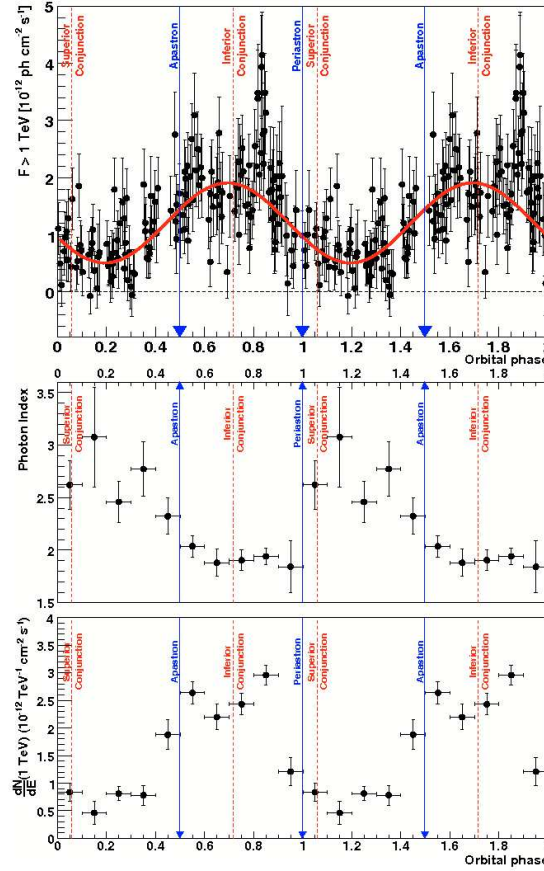


Fig. 11. At the top, the lightcurve of the photon flux above 1 TeV of LS 5039 presented by Aharonian et al. (2006). Two full phase periods are shown for clarity. The blue solid arrows depict periastron and apastron. The thin red dashed lines represent the superior and inferior conjunctions of the compact object, and the thick red dashed line depicts the Lomb-Scargle Sine coefficients for the period giving the highest Lomb-Scargle power (see Aharonian et al. 2006 for details). At the middle, the fitted pure power-law photon index (for energies 0.2 to 5 TeV) versus phase interval of width $\phi = 0.1$ is presented. At the bottom, the power-law normalization (at 1 TeV) versus phase interval of width $\Delta\phi = 0.1$ is shown.

~ 4 the former and between ~ 1.9 – 3.1 the latter, with the spectrum hardening when flux increases (Aharonian et al. ¹⁷). The observed lightcurve and VHE SED are shown in Figs. 11 and 12, respectively. The maximum of the emission takes place around phase 0.8, similarly as it seems to happen at X-rays. Also, sudden increases/hardening in the flux and spectrum on hour timescales could have been detected at phase ~ 0.85 (de Naurois et al. ¹²⁷), being similar to what has been mentioned above concerning sharp peaks in X-rays. The TeV emission from LS 5039 has been studied by several authors in the microquasar (e.g. Paredes et al. ⁷⁸) and the pulsar context (e.g. Dubus et al. ¹²⁸; Sierpowska-Bartosik & Torres ^{129,130}). A more general approach to study the VHE emission from LS 5039 has been recently carried out by Khangulyan et al. ⁸³.

In the following, we present the multiwavelength SED and the orbital VHE lightcurve computed with the model sketched above for LS 5039. The values given to the free parameters of the model are chosen with the intention to show that a simple leptonic model can roughly explain the observed features of the emission taking into account the TeV data and the phenomenology of the source. At this stage, no electromagnetic cascading should be introduced.

On the spectral energy distribution and orbital variability

In Fig. 13, for illustrative purposes, we show the synchrotron and IC SED for LS 5039 averaged over the orbital phase interval $0.9 > \phi > 0.45$, corresponding to the inferior conjunction of the compact object ($\phi = 0.72$). We use this format for a better comparison with the spectral results from observations (Aharonian et al. ¹⁷), shown also in the figure. For the very high energy spectrum in superior conjunction, see Khangulyan et al. ⁸³, fig. 23; at that phase interval, the synchrotron emission

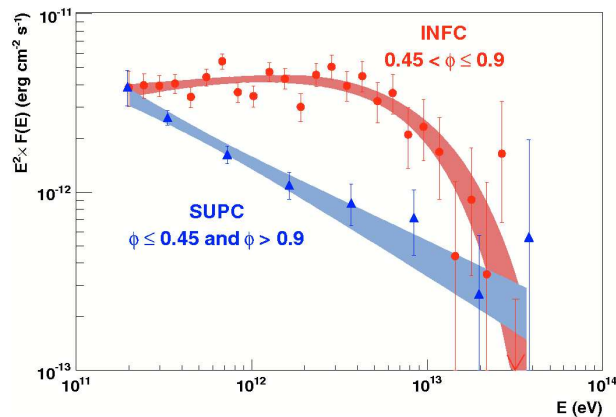


Fig. 12. Spectra of LS 5039 for the two broad orbital phase intervals $0.45 < \phi \leq 0.9$ (red circles), and $\phi \leq 0.45$ and $\phi > 0.9$ (blue triangles), from Aharonian et al. (2006). The shaded regions represent the 1σ confidence bands on the fitted functions (see Aharonian et al. 2006 for details).

will be similar to that at inferior conjunction. In Fig. 14, the VHE lightcurve along the orbit is shown. The adopted parameter values in both figures are the following: $V_{\text{adv}} = 0.1 c$, $Z_0 = 10^{12}$ cm, $i = 25^\circ$, $\eta = 10$ and $B = 0.05$ G. The exact values of B and V_{adv} are actually not crucial. In the case of B , its value just needs to fulfill acceleration constraints (i.e. to allow electrons to reach high enough energies to explain the TeV data), and be low enough such that VHE electrons will lose most of their energy via IC in the KN regime. Regarding V_{adv} , moderately different values will render similar results. To reach the observed emission levels, the total injected luminosity in relativistic electrons is $L_e \approx 1.5 \times 10^{35}$ erg s $^{-1}$. We note that we have computed the contribution from both the jet and the counter-jet and summed them up. Photon-photon absorption is taken into account. Remarkably, the synchrotron part of the spectrum is well below the observed fluxes, indicating that the dominant X-rays in this source likely come from a different emitting region. This region should be nevertheless physically connected to the TeV emitter, given the similar behavior in time of both the X-ray and the TeV radiation.

Regarding variability, we show in Fig. 14 the orbital VHE lightcurve obtained for the same parameter choice adopted to compute the SED. Although the matching with observations is not perfect, it is necessary to state that the lightcurve provided in Aharonian et al. ¹⁷ is constructed in bins with relatively small statistical significance, the spectra are simplified to pure power laws (and they could be more complicated than just a power law, as shown in Fig. 13), and includes data points from observations of very different epochs. In any case, just playing with propagation effects, IC scattering and photon photon absorption, one can already obtain very different lightcurves.

For an extensive discussion on the role of the different parameters present in the used model, we refer to Khangulyan et al. ⁸³. Here our purpose is just to note that the leptonic scenario, accounting for changes in the interaction geometry due to the orbital motion of the system, can reproduce quite nicely the observed spectra for different phases. It is worthy mentioning that, to reach the observed maximum photon energies, Z_0 is to be $\geq 10^{12}$ cm unless the acceleration efficiency is close to the maximum one, i.e. $\eta < 10^{\text{h}}$. In addition, the magnetic field in the accelerator/emitter is restricted to a relatively narrow band around 0.1 G.

4.3.2. *LS I +61 303*

LS I +61 303 is a quite eccentric ($e = 0.72$) HMXB, located at ≈ 2 kpc, with an orbital semi-major axis of $\approx 6 \times 10^{12}$ cm, a Be primary star of luminosity $\approx 10^{38}$ erg s $^{-1}$ and temperature ≈ 28000 K, and an orbital period of 26.4960 days (Hutchings & Crampton ¹³¹; Gregory ¹³²; Casares et al. ¹³³). The inclination of the system is not well constraint, being in the range $i = 15 - 60^\circ$. Massi et al. (^{134,135}) detected radio

^hIn the case of a deep emitter, the magnetic field in the system should be well below several G, as noted by Bosch-Ramon et al. ¹¹⁷.

jets, with apparently relativistic motion, at ~ 100 milliarcsecond scales and classified LS I +61 303 as a microquasar. Otherwise, the source does not show signatures of accretion in the X-rays (e.g. Sidoli et al. ¹³⁶; Paredes et al. ¹³⁷; and references therein), which are of likely non-thermal origin. This fact, altogether with other arguments -mainly related to the extended radio emission morphology (see Dhawan et al. ¹³⁸)- have let several authors to put forward a non-accreting pulsar as the compact object in the system (e.g. Dubus ¹³⁹; Chernyakova et al. ¹⁴⁰; Dhawan et al. ¹³⁸), which had been proposed for the first time by Maraschi & Treves ¹⁴¹. Nevertheless, the microquasar scenario cannot be discarded, and it may indeed explain some of the inferred properties of LS I +61 303 better than the pulsar scenario (e.g. Romero et al. ¹⁴²). In fact, the apparently slow and collimated radio structures detected in this source may be rather difficult to explain in the colliding wind context, in which very fast motions of the shocked pulsar wind could be expected (see Bogovalov et al. ¹⁴³). We recall that LS I +61 303 has been detected in the TeV range by MAGIC (Albert et al. ¹⁹) with the maximum around the phase 0.6, being not detected during periastron passage, at phase 0.23 (Casares et al. ¹³³). This source had been also detected by EGRET (Kniffen et al. ¹⁴⁴). It is worthy noting that the

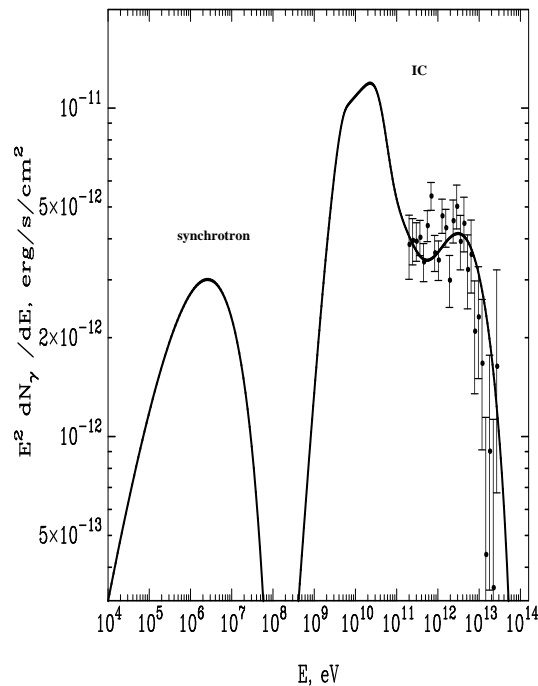


Fig. 13. Computed synchrotron and IC SED of LS 5039 averaged over the orbital phase interval $0.9 > \phi > 0.45$. The HESS data points are also shown (Aharonian et al. 2006). The adopted parameter values are $V_{\text{adv}} = 0.1c$, $Z_0 = 10^{12}$ cm, $i = 25^\circ$, $\eta = 10$, $B = 0.05$ G, and $L_e = 1.5 \times 10^{35}$ erg s $^{-1}$. The total contribution from the jet and the counter-jet is shown.

lightcurves in the radio, X-rays, and high-energy and very high-energy gamma-rays look somewhat similar (see fig. 3 in Chernyakova et al. ¹⁴⁰ and references therein). Several authors have adopted different frameworks and mechanisms to explain the high energy radiation from this source (in the microquasar framework: e.g. Romero et al. ¹⁴⁵ -hadronic-, Bosch-Ramon et al. ¹⁴⁶ -leptonic-, Bednarek ¹⁰¹ -cascading-; in the pulsar framework: e.g. Leahy ¹⁴⁷, Dubus ¹³⁹ -leptonic-, Chernyakova et al. ¹⁴⁰ -hadronic-; regarding neutrino detectability, see Christiansen et al. ¹⁴⁸ and Torres & Halzen ¹⁴⁹).

On the spectral energy distribution and orbital variability

In Fig. 15, we show the computed synchrotron and IC SED for LS I +61 303 at $\phi = 0.6$. The adopted parameter values are the following: $V_{\text{adv}} = 0.1 c$, $Z_0 = 10^{12}$ cm, $i = 30^\circ$, and $\eta = 10$. In this case, the magnetic field energy density could be larger than the radiation one compared to LS 5039, since the VHE spectrum is less hard, leaving more room for synchrotron losses (which yield a softer spectrum). The value of B obtained here to reproduce the observed radiation is 0.5 G. The total adopted L_e is 1.5×10^{35} erg s⁻¹. In LS I +61 303, the X-ray levels would not be far from the observed ones. Still, for the adopted magnetic field, adjusted to explain the TeV spectrum, the fluxes are still too low. Unlike LS 5039, neither

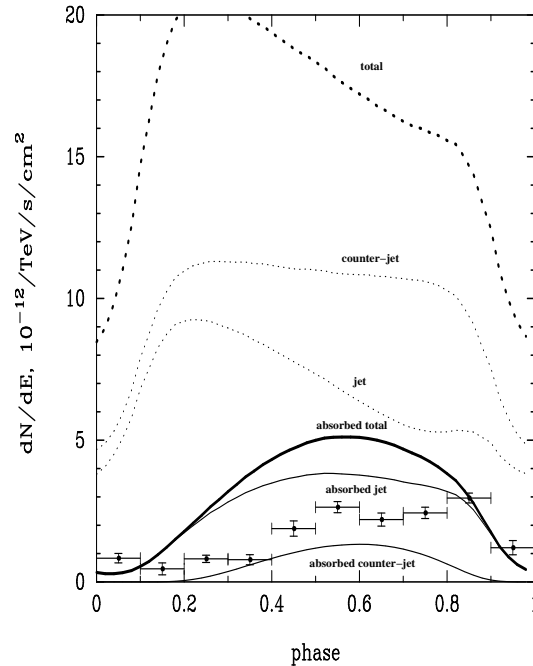


Fig. 14. Computed IC orbital lightcurve of the differential photon flux at 1 TeV for LS 5039. The different components, jet, counter-jet and summation of both, are labelled. The adopted parameters are the same as those adopted in Fig. 13.

the observer/binary system geometry nor the impact of photon-photon absorption are enough when understanding the TeV variability, given the distance to, and the luminosity of, the primary star. At the phase at which this emission is detected, the gamma-ray attenuation is low, and the IC scattering angle changes relatively little. In Figs. 16, 17, and 18, the differential photon flux lightcurves at 0.1, 1 and 10 TeV, respectively, are shown. In the observed lightcurve (Albert et al. ¹⁹), the maximum of the emission is at phases (using the ephemeris of Casares et al. ¹³³; see also Grundstrom et al. ¹⁵⁰) different from those predicted by our IC/photon-photon absorption model. This fact, plus the similarity of the VHE lightcurve with those at other wavelengths, suggest intrinsic changes of the emitting region. Interestingly, the 10 TeV emission in our scenario peaks roughly around periastron passage, due to the characteristics of the pair creation and IC cross sections.

5. Further comments

We have discussed in this work the different processes that may take place in microquasars, and explored the possibility that stellar IC scattering is behind the VHE radiation from three sources recently detected in the TeV range. We have shown also the importance of photon-photon absorption, whose occurrence can be used to constrain the emitter properties. In this section, we critically discuss three hot topics that are, in our view, very relevant for the kind of source discussed here. The first point is related to the possibility, already mentioned and commented above,

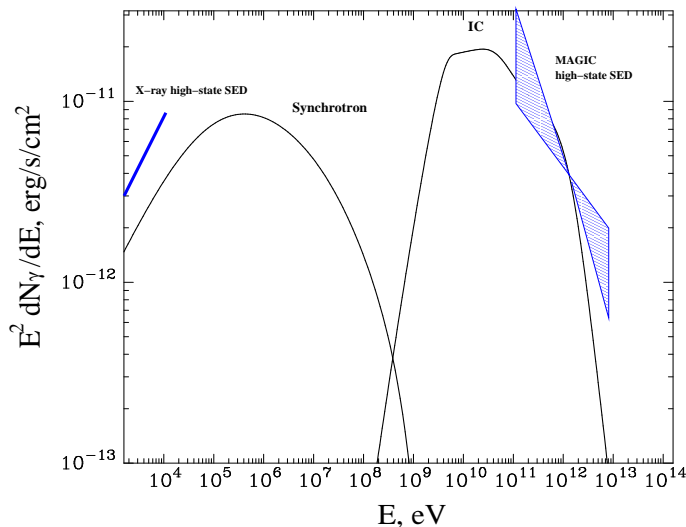


Fig. 15. The Computed Synchrotron and IC SED for LS I +61 303 at phase $\phi = 0.6$, together with the observed VHE SED, is shown. The adopted parameter values are $V_{\text{adv}} = 0.1 c$, $Z_0 = 10^{12}$ cm, $i = 30^\circ$, $\eta = 10$, $B = 0.5$ G and $L_e = 1.5 \times 10^{35}$ erg s⁻¹. The total contribution from the jet and the counter-jet is shown.

that a non-accreting pulsar may power the non-thermal broadband emission in LS I +61 303 and LS 5039. The second point, affecting Cygnus X-1 as well, is the role played by the companion star concerning high-energy processes and the dynamics of the jet. Finally, some comments are made regarding the prospects of the study of microquasars with the new/future VHE instrumentation.

5.1. Evidences for a pulsar nature

Although we do not consider here that LS I +61 303 and LS 5039 may harbor young non-accreting pulsars instead of an accreting black-hole, this possibility cannot be discarded. At present, the strongest argument in favor of this is the lack of accretion features in the X-ray spectrum. An *extension* of this argument is the fact that the timing properties of the X-ray emission in these two sources, and even the radio/X-ray behavior, do not correspond to what is believed a microquasar should be. Needless to say, this argument is phenomenological, and relies on a supposed regularity of the microquasar behavior at X-rays. The same could be said regarding the radio behavior and the radio/X-ray connection.

Indeed, there is a whole set of phenomenological studies, as already mentioned in Sect. 2, majorly grounded on observations but also to some extent on theoretical

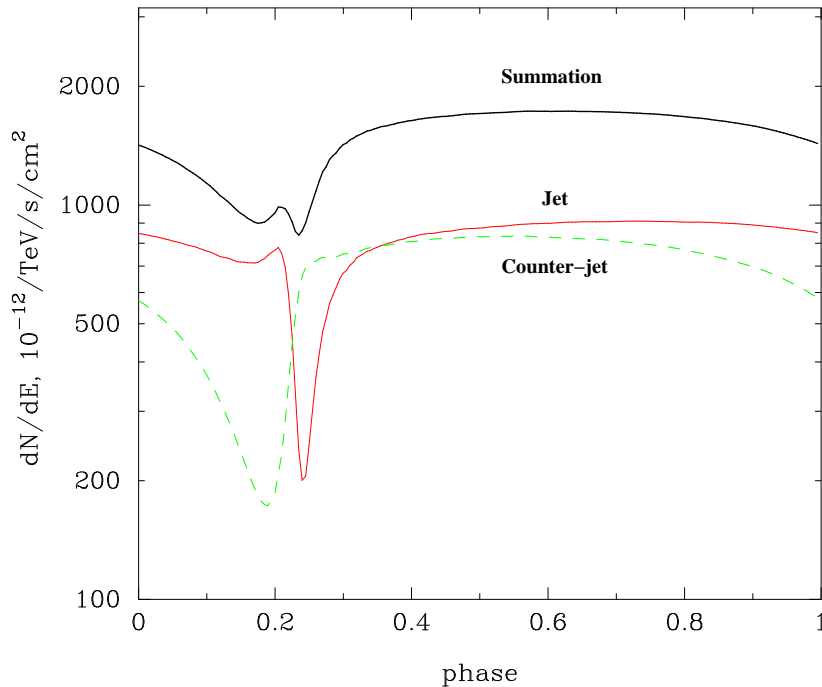


Fig. 16. The light-curve (differential photon flux) at 100 GeV for LS I +61 303. The jet and the counter-jet components are labelled. The adopted parameter values are the same as those in Fig. 15.

models, which try to give an unified microquasar picture. LS 5039 and LS I +61 303 do not fit in such a picture regarding the points mentioned above. Nevertheless, most of the high-mass microquasars, and to a lesser extent several low-mass microquasars, present some level of discrepancy from the standard picture, and not all the sources may have occurring in them the same mechanisms as those comprehended in the standard scenario. All this shows that such a picture or framework is a useful working hypothesis, but it cannot still be a discrimination tool when trying to find out whether or not a source pertains to some class of objects. In the same line, sometimes the morphology of the radio emission from these systems is used as an argument, again phenomenological, against their microquasar nature. In this regard, it is claimed that the extended radio emission does not fit the standard picture of microquasar jets. Nevertheless, it is worthy pointing out here that galactic compact jets are sometimes detected at the resolution limits of radio VLBI interferometers. It makes therefore difficult to argue, based on solid observational grounds, about how a microquasar jet should look like. From the theoretical point of view, to define how a canonical microquasar jet should be is presently not possible, since we lack a complete theory for jet formation and collimation, and there might be more than one mechanism operating.

There are otherwise two good indicators of the presence of a pulsar in the system, i.e. the detection of radio and X-ray pulsations, and the lack of strong X-ray

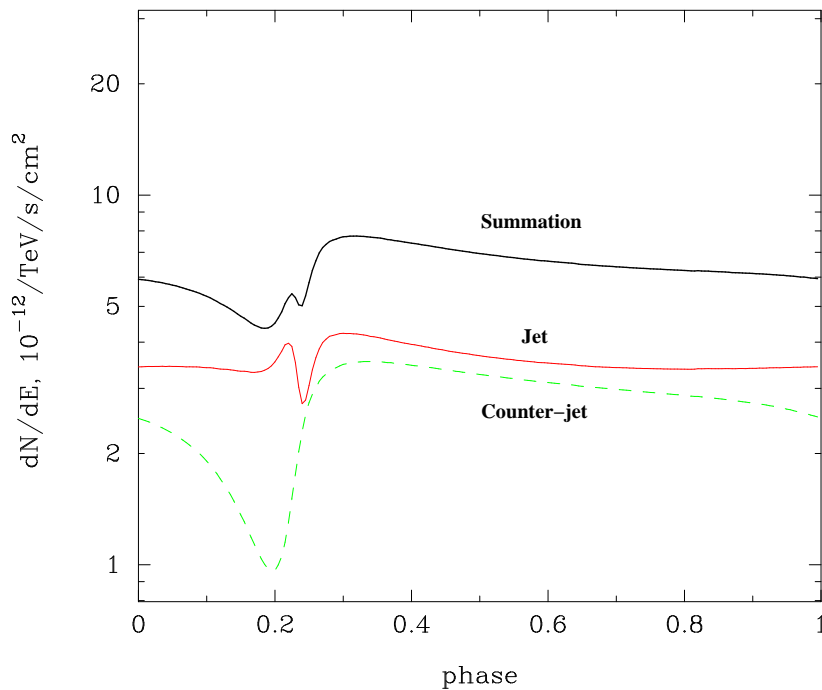


Fig. 17. The same as in Fig. 16 but at 1 TeV.

radiation (as is the case) due to any form of accretion onto a possible neutron star surface (in case the compact object were known to be a neutron star). To date, none of both questions has been answered. Neither pulsations have been detected, nor the problem of the compact object nature has been solved. The lack of pulsations may be explained by dense stellar wind ionized material smearing out the pulsed signal via free-free absorption, although the powerful pulsar wind would allow the observer to see the pulsar without the interference of the stellar wind around inferior conjunction. The radiation beam may also point away from us preventing us from seeing it. Regarding accretion X-ray bursts, since the masses of the components in LS 5039 and LS I +61 303 are not yet properly constraint, we cannot tell whether the compact object is a black hole or a neutron star.

Therefore, the question whether there is an accreting or a non-accreting compact object in LS 5039 and LS I +61 303 remains open. Fortunately, because of this fact, their complex multiwavelength spectral and temporal behavior, and their TeV detections, these two sources are extensively studied nowadays. This will bring for sure fruitful and surprising results in the near future.

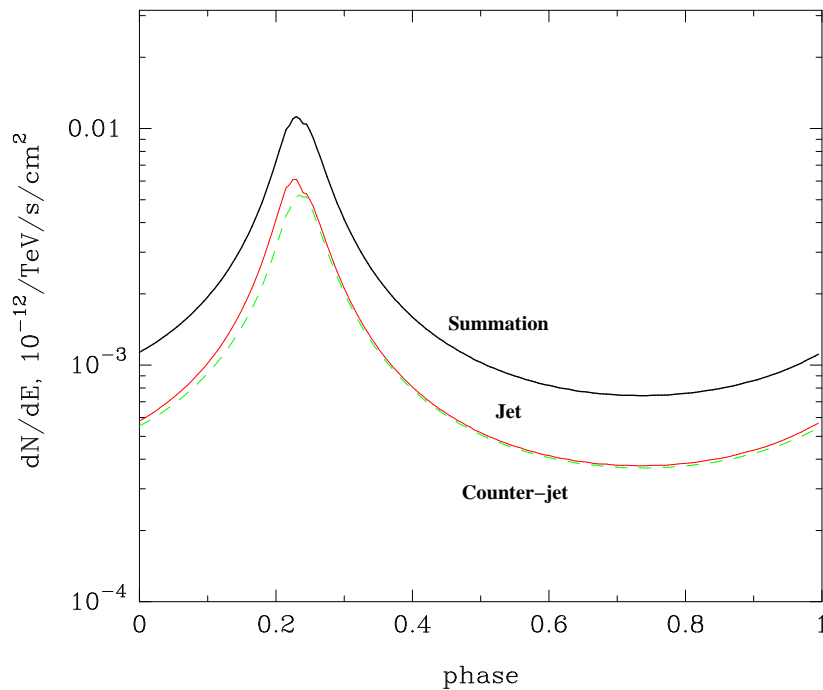


Fig. 18. The same as in Fig. 16 but at 10 TeV.

5.2. *The relevance of the primary star*

LS 5039, LS I +61 303, and Cygnus X-1 contain a massive and hot OB type star which embeds the jet/accelerator/emitter with dense matter and photon fields. Unlike low-mass microquasars, where the accretion/ejection phenomena could be naturally reduced to the disk/jet system, in high-mass microquasars (SS 433 and Cygnus X-3 are two additional instances of high-mass microquasars, both being certainly peculiar), the strong photon field should play an important role in the radiation processes via, e.g., stellar IC, photo-meson production and photo-disintegration, photon-photon absorption, secondary pair radiation and electromagnetic cascading. In addition, the strong stellar wind is likely to have an impact in the radiation processes via dynamical interactions with the jet/accelerator/emitter, providing targets for pp radiation, confining relativistic particles, either secondary pairs or protons, absorbing part of the radio and X-ray photons produced in the system, and determining the medium at large scales (and thereby influencing the processes that take place in the termination regions of the microquasar jets). As shown along this review, numerous studies have been or are being carried out to clarify the importance of the primary star in the mentioned processes.

Beside the fact that the physics to extract from theoretical studies plus present and future observations can teach us a lot about jets, acceleration and radiation processes, and stellar winds, it is also important to remark that the presence of the star cannot be neglected when modeling phenomenologically the observations of high-mass microquasars. It seems very likely that these systems cannot be understood as just accretion/ejection systems to first, or even zero, order of approximation, but require a much more complex approach including hydrodynamical and magnetohydrodynamical simulations of jets and their environment, a consistent treatment of acceleration and emission of particles, and the physics of OB stars and their winds.

5.3. *Prospects*

The future instruments like MAGIC II, HESS II, CTA, and the already on-flight GLAST will allow to make a big step in our understanding of microquasars and gamma-ray emitting binaries. The better performance at low energies of all these instruments will allow to study for instance the possible development of electromagnetic cascades (in case of weak magnetic fields) or the secondary single-scattering IC component, giving information on the physical conditions of the VHE emitter environment. Furthermore, radiation components below 100 GeV coming from regions invisible in TeV (e.g. due to severe absorption or maximum particle energy $\lesssim 100$ GeV), could also be investigated. The good sensitivity in the whole energy range would allow the study of fast variability and accurate modeling, which is of primary importance to understand the structure of the source, and the nature of the particles and processes behind the gamma-ray emission. Finally, an extension of the operation energy range up to ~ 100 TeV (e.g. CTA) would bring the opportunity to study in detail the acceleration processes with extreme efficiencies, like in the case

of LS 5039.

6. Summary

Microquasars are sources in which non-thermal processes occur. Particle acceleration is taking place in these systems, although the mechanisms involved are still unclear (e.g. non-relativistic and relativistic shocks, magnetic turbulence, magnetic reconnection, etc.). The complexity of such a multiwavelength emitters, in which different radiative processes may be relevant in the same energy range, and emission reprocessing via photon-photon absorption is common, yields the study in detail of the underlying physics quite difficult. Nevertheless, the detection of TeV photons can help to constrain the fundamental properties of the emitting region, since the relevant timescales are short. Because of this, Cherenkov astronomy is allowing for the first time to really probe the accelerator/emitter in microquasars. Cygnus X-1, observed by MAGIC, has been found flaring during phases when photon-photon absorption is expected to be very severe, giving information on the emitter location and the stellar magnetic field. LS 5039, detected by the Cherenkov telescope HESS as a periodical TeV emitter, is at the moment the best laboratory to understand particle acceleration and radiative processes in galactic compact sources. LS I 61 +303, detected as well by MAGIC, shows TeV emission that varies along the orbit. Since geometric effects would not play in this source a role for the orbital variability as important as in the case of LS 5039, intrinsic properties of the emitter should also change. The same would apply to Cygnus X-1.

We conclude that a leptonic scenario can explain the radiation from microquasars at very high energies, although hadronic emission, energetically very demanding, cannot be discarded. In case of LS 5039 and Cygnus X-1, acceleration of particles and emission seem to take place in the borders of the system. Due to their relatively hard VHE spectra, the emitter magnetic field in LS 5039 and LS I +61 303 should be low. Due to the magnetic field produced by an OB star, gamma-rays, although likely photon-photon absorbed, can hardly trigger efficient electromagnetic cascades and secondary energy may be radiated mainly via the synchrotron process.

TeV microquasars are showing us that they behave in a different way from their extragalactic analogs, the blazars, being very much affected by the presence of the primary star and the the orbital motion.

Acknowledgments

The authors thank the anonymous referee for constructive comments and useful suggestions. The authors are grateful to Felix A. Aharonian for fruitful discussion and advice. The authors thank Anabella T. Araudo for helping to improve the manuscript. V.B-R. gratefully acknowledges support from the Alexander von Humboldt Foundation. V.B-R. acknowledges support by DGI of MEC under grant AYA2007-68034-C03-01, as well as partial support by the European Regional Development Fund (ERDF/FEDER).

7. References

References

1. Mirabel, I. F. & Rodríguez, L. F. *ARA&A* **37**, 409 (1999)
2. McClintock, J. E., Remillard, R. A. Black Hole Binaries in *Compact stellar X-ray sources*, eds. W. Lewin & M. van der Klis (Cambridge University Press) (2006)
3. Fender, R. P., Belloni, T. M., Gallo, E. *MNRAS*, **355**, 1105 (2004)
4. Gallo E., Fender R. P., Pooley G. G. *MNRAS*, **344**, 60 (2003)
5. Corbel, S., Nowak, M. A., Fender, R. P., Tzioumis, A. K., Markoff, S. *A&A*, **400**, 1007 (2003)
6. Fender, R. P., Gallo, E., Jonker, P. G. *MNRAS* **343**, 99 (2003)
7. Ribó, M. in *Future Directions in High Resolution Astronomy: The 10th Anniversary of the VLBA*, (ASPC, 2005) 340, 421 [astro-ph/0402134]
8. Corbel, S., Fender, R. P., Tzioumis, A. K., *et al.*, *Science* **298**, 196 (2002)
9. Bosch-Ramon, V., *Ap&SS* **309**, 321 (2007)
10. Fender, R. *NewAR* **48**, 1399 (2004)
11. Chaty, S., Haswell, C. A., Malzac, J. *MNRAS* **346**, 689 (2003)
12. Levinson, A. & Blandford, R. D. *ApJ* **456**, L29 (1996)
13. Levinson, A. & Mattox, J. R. *ApJ*, **462**, 67 (1996)
14. Paredes, J.M., Martí, J., Ribó, M., Massi, M., *Science* **288**, 2340 (2000)
15. Albert, J. *et al.* *ApJ* **665**, L51 (2007)
16. Aharonian, *et al.* *Science* **309**, 746 (2005)
17. Aharonian, F. A. *et al.* *A&A* **460**, 743 (2006)
18. Casares, J., Ribó, M., Ribas, I., *et al.*, *MNRAS* **364**, 899 (2005)
19. Albert, J. *et al.* *Science* **312**, 1771 (2006)
20. Mirabel I. F., Rodríguez L. F., Cordier B., Paul J., Lebrun F., *Nature* **358**, 215 (1992)
21. Mirabel, I. F. & Rodríguez, L. F. *Nature* **371**, 46 (1994)
22. Merloni, A., Heinz, S., di Matteo, T. *MNRAS* **345**, 1057 (2003)
23. Falcke, H., Krding, E., Markoff, S., *A&A* **414**, 895 (2004)
24. Körding, E., Falcke, H., Corbel, S. *A&A* **456**, 439 (2006)
25. Markoff, S., Nowak, M. A., Wilms, J., *ApJ* **635**, 1203 (2005)
26. Maccarone, T. J., *MNRAS* **360**, L68 (2005)
27. Bogovalov, S. V. & Kelner, S. R. *Astron. Rep.* **49**, 57 (2005)
28. Levinson, A. *Int. J. Mod. Phys. A* **21**, 30 (2006)
29. Araudo, A. T., Romero, G. E., Bosch-Ramon, V., Paredes, J. M. *A&A* **476**, 1289 (2007)
30. Blandford, R. D. *MNRAS* **176** 465 (1976)
31. Blandford, R. D. & Znajek, R. L. *MNRAS* **179**, 433 (1977)
32. Blandford, R. D. & Payne, D. G. *MNRAS* **199**, 883 (1982)
33. Meier, D. *ApJ*, **459**, 185 (1996)
34. Koide, S., Shibata, K., Kudoh, T., Meier, D. L. *Science* **295**, 1688 (2002)
35. Chattopadhyay, I. & Chakrabarti, S. K. *MNRAS* **333**, 454 (2002)
36. Meier, D. *NewA Rev.*, **47**, 667 (2003)
37. Hujeirat, A. *A&A* **416**, 423–435 (2004)
38. Meier, D. L. *Ap&SS* **300**, 55 (2005)
39. De Villiers, J.-P., Hawley, J. F., Krolik, J. H., Hirose, S. *ApJ* **620**, 878 (2005)
40. Ferreira, J., Petrucci, P. O., Henri, G., Saug, L., Pelletier, G. *A&A* **447**, 813 (2006)
41. McKinney, J. C. *MNRAS*, **368**, 1561 (2006)
42. Hawley, J. F. & Krolik, J. H. *ApJ* **641**, 103 (2006)
43. Komissarov, S. S., Barkov, M. V., Vlahakis, N., Königl, A. *MNRAS* **380**, 51 (2007)

44. Barkov, M. V. & Komissarov, Serguei S. *MNRAS* **385**, 28 (2008)
45. Junor, W., Biretta, J. A., Livio, M. *Nature* **401**, 891 (1999)
46. Horiuchi, S., Meier, D. L., Preston, R. A., Tingay, S. J. *PASJ* **58**, 221 (2006)
47. Namiki, M., Kawai, N., Kotani, T., Makishima, K., *PASJ* **55**, 281 (2003)
48. Hardee, P. E., Hughes, P. A. *ApJ* **583**, 116 (2003)
49. Tsinganos, K., Vlahakis, N., Bogovalov, S. V., Sauty, C., Trussoni, E. *Ap&SS* **293**, 55 (2004)
50. Perucho, M. & Bosch-Ramon, V. *A&A* **482**, 917 (2008)
51. Fanaroff, B. L. & Riley, J. M. *MNRAS* **167**, 31 (1974)
52. Perucho, M. & Martí, J. M. *MNRAS* **382**, 526 (2007)
53. Kaiser, C. R. & Alexander, P. *MNRAS* **286**, 215 (1997)
54. Scheck, L., Aloy, M.A., Martí, J.M^a, Gómez, J.L., Müller, E. *MNRAS* **331**, 615 (2002)
55. Zealey, W. J., Dopita, M. A., Malin, D. F. *MNRAS* **192**, 731 (1980)
56. Velázquez, P. F. & Raga, A. C. *A&A*, **362**, 780 (2000)
57. Sikora, M., Begelman, M. C., M., Greg M., Lasota, J. P., *ApJ* **625**, 72 (2005)
58. Zenitani, S., Hoshino, M., *ApJ* **562**, 63 (2001)
59. Derishev, E. V., Aharonian, F. A., Kocharovskiy, V. V., Kocharovskiy, V. V., *PhRvD* **68**, 3003 (2003)
60. Stern, B., Poutanen, J. *MNRAS* **372**, 1217 (2006)
61. Gierliński, M., Done, C., *MNRAS* **342**, 1083 (2003)
62. Neronov, A. & Aharonian, F. A. *ApJ* **671**, 85 (2007)
63. Rieger, F. & Aharonian, F. A. *A&A* **479**, L5 (2008)
64. Drury, L. O., *Rep. Prog. Phys.* **46**, 973 (1983)
65. Fermi, E., *Phys. Rev.* **75**, 1169 (1949)
66. Rieger, F. M.; Duffy, P., *ApJ* **617**, 155 (2004)
67. Rieger, F. M., Bosch-Ramon, V., Duffy, P. *Ap&SS* **309**, 119 (2007)
68. Heinz, S., Sunyaev, R., *A&A* **390**, 751 (2002)
69. Markoff S., Falcke H., Fender R., *A&A* **372**, 25 (2001)
70. Bosch-Ramon, V., Romero, G E., Paredes, J. M. *A&A* **447**, 263 (2006)
71. Bosch-Ramon, V., Paredes, J. M., *A&A* **417**, 1075 (2004)
72. Romero, G. E., Kaufman Bernadó, M. M., Mirabel, I. F., *A&A* **393**, 61 (2002)
73. Georganopoulos, M., Aharonian, F. A., Kirk, J. G., *A&A* **388**, 25 (2002)
74. Levinson, A., Waxman, E. *PhRvL* **87**, 171101 (2001)
75. Aharonian, F. A., Anchordoqui, L. A., Khangulyan, D., Montaruli, T. *J.Phys.Conf.Ser.* **39** 408 (2006)
76. Romero, G. E. & Vila G. S. *A&A* **485**, 623 (2008)
77. Yuan, F.; Cui, W., Narayan, R., *ApJ* **620**, 905 (2005)
78. Paredes, J. M., Bosch-Ramon, V., Romero, G. E., *A&A* **451**, 259 (2006)
79. Atoyan, A. M., Aharonian, F. A., *MNRAS* **302**, 253 (1999)
80. Dermer, C., Böttcher, M., *ApJ* **643**, 1081 (2006)
81. Paredes, J. M., Ribó, M., Martí, J., *A&A* **393**, 99 (2002)
82. Kaufman Bernadó M.M., Romero G.E., Mirabel I.F., *A&A* **385**, 10 (2002)
83. Khangulyan, D., Aharonian, F., Bosch-Ramon, V., *MNRAS*, **383**, 467 (2008)
84. Romero, G. E., Torres, D. F., Kaufman Bernadó, M. M., Mirabel, I. F., *A&A* **410**, 1 (2003)
85. Romero, G. E., Orellana, M., *A&A* **439**, 237 (2005)
86. Aharonian, F. Invited talk at *The International Conference on Neutrino Physics and Astrophysics* (2006) [astro-ph/0702680]
87. Bednarek, W. *ApJ* **631**, 466 (2005)
88. van der Laan, H., *Nature* **211**, 1131 (1966)

40 *V. Bosch-Ramon & D. Khangulyan*

89. Aharonian, F. A.; Atoyan, A. M. *NewAR* **42**, 579 (1998)
90. Bordas, P., Bosch-Ramon, V., Paredes, J. M. *Int. J. Mod Phys. D* **17**, 1895 (2008)
91. Bosch-Ramon, V., Aharonian, F. A., Paredes, J. M., *A&A* **432**, 609 (2005c)
92. Akharonian, F. A., Vardanian, V. V., *Ap&SS* **115**, 31 (1985)
93. Donati, J. F., Babel, J., Harries, T. J. et al. *MNRAS* **33**, 55 (2002)
94. Protheroe, R. J. & Stanev, T. , *ApJ* **322**, 838 (1987)
95. Moskalenko I.V., Karakula S., *ApJS* **92**, 567 (1994)
96. Bednarek, W. *A&A*, **322**, 523 (1997)
97. Bttcher, M., Dermer, C. D. *ApJ*, **634**, L81 (2005)
98. Böttcher, M., Dermer, C., *ApJ* **634**, 81 (2005)
99. Dubus, G., *A&A* **451**, 9 (2006)
100. Reynoso, M. M., Christiansen, H. R., Romero, G. E. *Astrop. Phys.* **28**, 565 (2008)
101. Bednarek, W., *MNRAS* **368**, 579 (2006)
102. Orellana, M., Bordas, P., Bosch-Ramon, V., Romero, G. E., Paredes, J. M. *A&A* **476**, 9 (2007)
103. Bosch-Ramon, V., Khangulyan, D., Aharonian, F. A. *A&A* **482**, 397 (2008)
104. Hillas, A. M. *ARA&A* **22** 425 (1984)
105. Protheroe, R. J. Acceleration and Interaction of Ultra High Energy Cosmic Rays in *Topics in cosmic-ray astrophysics*, eds. M. A. DuVernois (Nova Science Publishing) (1999) [astro-ph/9812055]
106. Kelner, S. R., Aharonian, F. A., Bugayov, V. V. *Phys. Rev. D* **74**, 4018 (2006)
107. Kelner, S. R. & Aharonian, F. A. *Phys. Rev. D* **78**, 4013 (2008)
108. Aharonian F. A. & Heinzlmann, G. *Nucl. Phys. Proc. Suppl.* **60**, 193 (1998)
109. Rovero A. C. et al., *BAAA* **45**, 66 (2002)
110. Khangulyan, D. & Aharonian, F. A. in *High Energy Gamma-Ray Astronomy*, (AIP Conference Proceedings 2005), 745, 359 [astro-ph/0503499]
111. Stirling, A. M., Spencer, R. E., de la Force, C. J. *MNRAS*, **327**, 1273 (2001)
112. Ziolkowski, J. *MNRAS*, **358**, 851 (2005)
113. Gies, D. R., & Bolton, C. T. *ApJ*, **304**, 371 (1986)
114. Bednarek, W. & Giovannelli, F. *A&A* **464**, 437 (2007)
115. Sunyaev, R. A., & Truemper, J. *Nature* **279**, 506 (1979)
116. McConnell, M. L., Zdziarski, A. A., Bennett, K. *ApJ* **572**, 984 (2002)
117. Bosch-Ramon, V., Khangulyan, D., Aharonian, F. A. *A&A* **489**, L21 (2008)
118. Motch, C., Haberl, F., Dennerl, K., Pakull, M., Janot-Pacheco, E., *A&A* **323**, 853 (1997)
119. Bosch-Ramon, V., Paredes, J. M., Ribó, M. et al. *ApJ* **628**, 388 (2005)
120. Martocchia, A., Motch, C., Negueruela, I., *A&A* **430**, 245 (2005)
121. Ribó, M., Reig, P., Martí, J., Paredes, J. M., *A&A*, **347**, 518 (1999)
122. Ribó, M., Paredes, J. M., Moldon, J., Martí, J., Massi, M. *A&A* **481**, 17 (2008)
123. Ribó, M. Ph. D. Thesis, Universitat de Barcelona (2002)
124. Martí, J., Paredes, J. M., Ribó, M., *A&A* **338**, 71 (1998)
125. Horns, D., for the HESS collaboration, talk presented in 2nd Workshop On TeV Particle Astrophysics (2006)
126. Bosch-Ramon, V., Motch, C., Ribó, M., et al. *A&A* **473**, 545 (2007)
127. de Naurois, M. for the HESS collaboration, talk presented in The keV to TeV connection (2006)
128. Dubus, G., Cerutti, B., Henri, G. *A&A* **477**, 691 (2008)
129. Sierpowska-Bartosik, A., Torres, D. F. *ApJL*, **671**, 145 (2007)
130. Sierpowska-Bartosik, A., Torres, D. F. *ApJL*, **674**, 89 (2008)
131. Hutchings, J. B. & Crampton, D. *PASP* **93**, 486 (1981)

132. Gregory, P. C. *ApJ*, **575**, 427 (2002)
133. Casares, J., Ribas, I., Paredes, J. M., Martí, J., Allende Prieto, C. *MNRAS* **360**, 1105 (2005)
134. Massi, M., Ribó, M., Paredes, J. M., Peracaula, M., Estalella, R. *A&A* **376**, 217 (2001)
135. Massi, M., Ribó, M., Paredes, J. M., et al. *A&A* **414**, L1 (2004)
136. Sidoli, L., Pellizzoni, A., Vercellone, S., et al. *A&A* **459**, 901 (2006)
137. Paredes, J. M., Ribó, M., Bosch-Ramon, V., et al. *ApJ* **664**, 39 (2007)
138. Dhawan, V., Mioduszewski, A., Rupen, M. The VI Microquasar Workshop: Microquasars and Beyond (Proceedings of Science), 52, 1 (2006)
139. Dubus, G. *A&A* **456**, 801 (2006)
140. Chernyakova, M., Neronov, A., Walter, R. *MNRAS* **372**, 1585 (2006)
141. Maraschi, L. & Treves, A. *MNRAS* **194**, 1 (1981)
142. Romero, G. E., Okazaki, A. T., Orellana, M., Owocki, S. P. *A&A* **474**, 15 (2007)
143. Bogovalov, S. V., Khangulyan, D., Koldoba, A. V., Ustyugova, G. V., Aharonian, F. A. *MNRAS* **387**, 63 (2008)
144. Kniffen, D. A., Alberts, W. C. K., Bertsch, D. L. et al. *ApJ* **486** 126 (1997)
145. Romero, G. E., Christiansen, H. R., Orellana, M. *ApJ* **632**, 1093 (2005)
146. Bosch-Ramon, V., Paredes, J. M., Romero, G. E., Ribó, M. *A&A* **459**, L25 (2006)
147. Leahy, D. A., *A&A*, **413**, L1019 (2004)
148. Christiansen, H. R., Orellana, M., Romero, G. E. *Phys. Rev. D.* **73**, 3012 (2006)
149. Torres, D. F. & Halzen F. *Astropart.Phys.* **27**, 500 (2007)
150. Grundstrom, E. D., Caballero-Nieves, S. M., Gies, D. R. et al. *ApJ* **656**, 437 (2007)